TALLINN UNIVERSITY OF TECHNOLOGY
SCHOOL OF ENGINEERING
Department of Electrical Power Engineering and Mechatronics

SENSORLESS FIELD-ORIENTED CONTROL BASED ELECTRONIC SPEED CONTROLLER FOR CORELESS ELECTRICAL MACHINES

ANDURIVABA VÄLJAVEKTORJUHTIMISE KIIRUSE KONTROLLER RAUAVABADELE ELEKTRIMASINATELE

MASTER'S THESIS

Student: Robert Seredenko

Student code: 221941MAHM

Supervisor: Martin Sarap, Early-Stage Researcher

Tallinn 2025

(On the reverse side of title page)

AUTHOR'S DECLARATION

Hereby I declare, that I have written this thesis independently.
No academic degree has been applied for based on this material. All works, major viewpoints and data of the other authors used in this thesis have been referenced.

"....." ..... 20…..

Author: .....
/ signature /

Thesis is in accordance with terms and requirements

"....." ..... 20…..

Supervisor: .....
/ signature /

Accepted for defence

"....."..... 20… .

Chairman of theses defence commission: .....
/ name and signature /

Non-exclusive licence for reproduction and publication of a graduation thesis[1]

I, Robert Seredenko herby

1. Grant Tallinn University of Technology free license (non-exclusive) for my thesis "Sensorless Field-Oriented Control based Electronic Speed Controller for Coreless Electrical Machines",

supervised by Martin Sarap

1.1 to be reproduced for the purposes of preservation and electronic publication of the graduation thesis, incl. to be entered in the digital collection of the library of Tallinn University of Technology (TalTech) until expiry of the term of copyright;

1.2 to be published via the web of Tallinn University of Technology, incl. to be entered in the digital collection of the library of Tallinn University of Technology until expiry of the term of copyright.

2. I am aware that the author also retains the rights specified in clause 1 of the non-exclusive licence.

3. I confirm that granting the non-exclusive licence does not infringe other persons' intellectual property rights, the rights arising from the Personal Data Protection Act or rights arising from other legislation.

19.12.2024

---

[1] *The non-exclusive licence is not valid during the validity of access restriction indicated in the student's application for restriction on access to the graduation thesis that has been signed by the school's dean, except in case of the university's right to reproduce the thesis for preservation purposes only. If a graduation thesis is based on the joint creative activity of two or more persons and the co-author(s) has/have not granted, by the set deadline, the student defending his/her graduation thesis consent to reproduce and publish the graduation thesis in compliance with clauses 1.1 and 1.2 of the non-exclusive licence, the non-exclusive license shall not be valid for the period.*

Department of Electrical Power Engineering and Mechatronics

THESIS TASK

Student: Robert Seredenko, 211941MAHM
Study programme, main speciality: MAHM, Mechatronics
Supervisor: Martin Sarap, Researcher

Thesis topic:
(in English) Sensorless Field-Oriented Control based Electronic Speed Controller for Coreless Electrical Machines
(in Estonian) Andurivaba väljavektorjuhtimise kiiruse kontroller rauavabadele elektrimasinatele

Thesis main objectives:

1. Design and prototype an open-source ESC capable of performing sensorless field-oriented control with hardware features comparable to commercially available low cost ESCs.
2. Perform simple ESC design verification and validate ESC on a prototype coreless RFPM machine.
3. Compare ESC performance and system efficiency to commercially available low cost 6-step ESC.

Thesis task and schedule:

No	Task description	Deadline
1.	Literature review	15.09.2024
2.	Prototype ESC design and manufacturing	15.10.2024
3.	Prototype ESC design bring-up, verification and initial measurements	1.11.2024
4.	Measurements completed and initial thesis draft	1.12.2024
5.	Thesis complete and approved by supervisor	15.12.2024

Language: English **Deadline for submission of thesis:** "19" December 2024

Student: …….. ..... "....."..... 20…..a
/signature/

Supervisor: …….. ..... "....."..... 20…..a
/signature/

Head of study programme:
…….. ..... "....."..... 20…..a
/signature/

CONTENTS

PREFACE 7

LIST OF ABBREVIATIONS AND SYMBOLS 8

INTRODUCTION 9

1 LITERATURE REVIEW 11

1.1 BLDC and PMSM differences 11
1.2 Coreless BLDC and its advantages 12
1.3 BLDC machine control approach 13
1.3.1 Trapezoidal commutation 13
1.3.2 Sinusoidal commutation 16
1.3.3 Space Vector Modulation and third harmonic injection 17
1.3.4 Field Oriented Control 20
1.3.5 Control approach summary 24
1.4 Electronic Speed controller 24
1.5 Existing ESC solutions 26
1.5.1 ESC classification by Degree of Openness 26
1.5.2 ESC classification by current capability 27

2 ESC PROTOTYPE DESIGN 28

2.1 Proposed solution 28
2.2 Prototype ESC specifications 29
2.3 Component selection 31
2.3.1 Microprocessor 31
2.3.2 3-Phase inverter 32
2.3.3 Auxiliary converter 33
2.3.4 PCB temperature sensor 33
2.3.5 Status LED 34
2.4 ESC mathematical modelling 34
2.4.1 ESC Simulink simulation 34
2.4.2 DRV8316C thermal calculations 35
2.5 ESC PCB design 38
2.5.1 PCB schematic 38
2.5.2 PCB layout and routing 39
2.6 ESC Firmware 39

3 DESIGN VERIFICATION AND EXPERIMENTS 41

3.1 Prototype ESC design verification 41
3.1.1 Design verification setup 41
3.1.2 Design verification results 42
3.2 Experimental results 46
3.2.1 ESC input power and efficiency measurement setup 46
3.2.2 ESC input power and efficiency measurement results 49
3.3 Result analysis 54
3.4 Future improvements to prototype FOC ESC and experiments 55
3.4.1 Microcontroller choice 55
3.4.2 DRV8316C Motor Driver IC choice 56
3.4.3 Improvements to experiment setup 57

4 CONCLUSION 58

KOKKUVÕTE 60

REFERENCES 62

APPENDICES 65

Appendix 1 ESC schematic.....65
Appendix 2 MATLAB Simulink model of 6-step and FOC ESC.....66
Appendix 3 GitHub repository for prototype FOC ESC 67

PREFACE

I would like to express my sincere gratitude to my supervisor, Martin Sarap, for proposing the thesis topic and for his invaluable guidance and mentorship throughout this process. I would also like to thank the members of the Mechatronics and Autonomous Systems Research Group for their support, insightful discussions, and assistance during the course of this work.

LIST OF ABBREVIATIONS AND SYMBOLS

AC – Alternating Current

ADC – Analog to Digital Converter

AFPM - Axial flux permanent magnet, machine part is often excluded

Back-EMF – back-electromotive force, also known as counter-electromotive force

BLDC – Brushless direct current machine, machine part is often excluded

DC – Direct current

DMM – Digital multimeter

ESC – Electronic speed controller

FOC – Field-Oriented Control

GPIO – General purpose input output

IC – Integrated circuit

MCU – Microcontroller unit

MOSFET – Metal-oxide-semiconductor field-effect transistor

PID – Proportional, Integral, Differential control loop

PM – Permanent magnets

PMSM – Permanent magnet synchronous machine

PWM – Pulse width modulation

RFPM - Radial flux permanent magnet, machine part is often excluded

rpm– rotations per minute

UAV – Unmanned aerial vehicle

UV – Unmanned vehicle

VSD – Variable speed drive

INTRODUCTION

Brushless direct current (BLDC) machines are widely popular in a wide range of applications [1], including use in unmanned aerial vehicles (UAV) [2]. BLDC machines offer attractive set of advantages especially desired in UAV like quick dynamic response, high power density, high speed and efficiency, compact structure and low weight [1] [3] [4].

As rotor speeds up to 15000 rpm are necessary to drive the propellers efficiently, high pole count is still required for high torque density [5]. To satisfy these requirements, both the electrical machine and accompanying driver must be carefully designed to work together at this high of a speed. While high efficiency of BLDCs is largely driven by the elimination of field excitation losses and reduction in rotor losses [6], stator core losses and cogging torque ripple [6] present multitude of challenges when designing high speed machine with conventional stator core.

Stator core losses constitute the most important limitation in high-frequency and in turn high-speed operation [7]. Multiple approaches exist to lower the effect of stator core losses. One approach focuses on mitigation by using soft magnetic composite materials, improved stator material, thinner lamination or slotless stator configuration. Second approach instead completely eliminates core losses by using a coreless stator configuration. This approach can be readily implemented in an axial flux permanent magnet (AFPM) [5] [8] or on 3D printed radial flux permanent magnet (RFPM) machines. However, its adoption for high-speed applications remains limited and there is a lack of research regarding its use in UAVs.

While there has been extensive research done for BLDC control and commutation method improvements [3] [9] [10], academic focus has been largely on a kW scale. Low power (<100 W) scale has had little research done, especially on coreless BLDCs. This is exact scale, which could be applied to small scale UAVs. Currently most widespread available hobby grade Electronic Speed Controllers (ESC) in this power range are using simple sensorless 6-step commutation approach. While this approach can achieve very high speed, doesn't require special hardware and is computationally simple, it inherently has large torque ripple and high acoustically noise compared to other commutation methods [4].

To achieve the best performance and efficiency, the drive current should closely match the back-EMF waveform of the BLDC machine [11]. Although the six-step commutation works well with traditional BLDC machine due to both having trapezoidal shaped back-

EMF, the back-EMF of coreless BLDC machine is sinusoidal shape due to lack of iron core. To achieve sinusoidal shaped drive current, either sinusoidal commutation or Field-Oriented Control (FOC) must be employed.

Previously FOC was not achievable by small microcontrollers (MCU) due to large amount of computational power needed [12]. As there has been noticeable advancement in DSP and MCU technology in recent years, it has enabled advanced motor control approaches like FOC to be done on cheaper and smaller DSPs and MCUs. These have shown to have enough computational power to perform sensorless FOC with current control [13].

The aim of this thesis is to design and prototype an open-source ESC capable of performing sensorless FOC and includes hardware feature parity with commercially available low cost ESCs. Author's ESC is then verified on a prototype coreless RFPM machine and system input power consumption is compared to the commercially available low cost 6-step ESC.

The first chapter of the thesis provides short overview about the BLDC machine and different stator configurations relevant to the thesis, a detailed literature review about BLDC control approaches and provides background information about the components used in ESC, its structure and proposes two classifications for existing ESCs on the market. Second chapter handles all the steps required for a complete design of an ESC, from setting the specifications and choice of components to the electrical simulations and thermal calculations. Fourth and last chapter includes prototype FOC ESC design verification and input power consumption comparison study between prototype FOC ESC and comparable commercially available 6-step ESC.

1 LITERATURE REVIEW

Brushless direct current (BLDC) machine is a subtype of the Permanent Magnet Synchronous Machines (PMSM). BLDC machines commonly have 3 stator phases in wye configuration and rotor with permanent magnets (see Figure 1.1). By varying the winding and pole count, BLDC machine torque and speed can be adjusted for an individual application. [14]

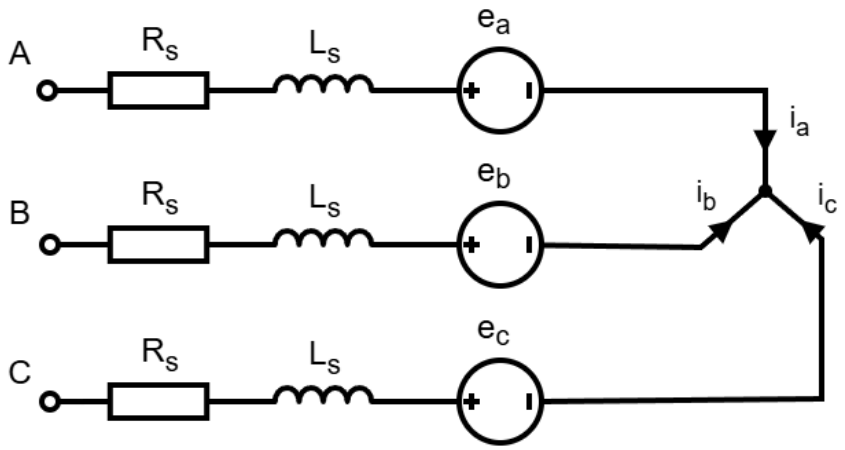

Figure 1.1 BLDC and PMSM machine equivalent circuit [10]

1.1 BLDC and PMSM differences

A typical BLDC machine differs from other PMSMs by the shape of the back-EMF. BLDCs historically have had back-EMF in shape of trapezoid, instead of sinusoidal back-EMF as is in case with PMSMs. This difference appeared, because historically the BLDC motor controllers with trapezoidal commutation strategy were significantly cheaper and easier to manufacture than other more complex and advanced commutation strategies. This resulted in BLDCs having winding distribution adjusted for trapezoidal shape, as highest efficiency is achieved by using same control waveform as the back-EMF shape [11].

It is necessary to mention that there is nothing preventing the use of trapezoidal commutation on PMSM and vice-versa to get benefit of different commutation, but the benefit gains won't be equal to the machine using commutation optimized for particular winding distribution and back-EMF.

Table 1.1 Characteristics comparison between typical PMSM and BLDC [12]

	Typical PMSM	**Typical BLDC**
Back-EMF Waveform	Sinusoidal	Trapezoidal
Winding distribution	Sinusoidal	Trapezoidal
Energized phase count	Three Phases	Two Phases

1.2 Coreless BLDC and its advantages

BLDC machines can be characterized by widely of factors, but main characterization relevant for this thesis is the stator type. Three main types of stators are slotted laminated iron core, slotless and coreless stator.

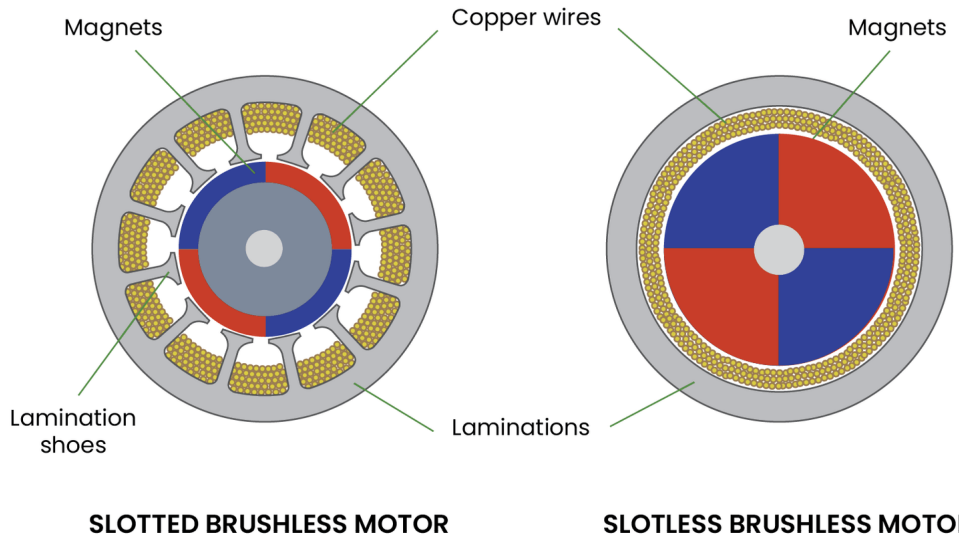

Figure 1.2 Slotted and slotless motors example [15]

The most widespread stator type on BLDC machine is laminated iron core type. The iron core is used to substantially increase stator coil inductance and in turn the stator flux linkage and machine torque. This enables to use fewer permanent magnets (PM) in rotors or less turns in stator to achieve target torque. But the use of iron core comes with challenges like cogging torque [6], hysteresis and eddy current losses in the stator [16]. Although all previous mentioned issues can be reduced with appropriate techniques and precautions, at high rotational speeds these losses become increasingly problematic as hysteresis losses scales proportional to frequency and eddy current losses square of frequency.

Another approach to tackle the cogging torque, hysteresis and eddy currents is the use of slotless or coreless stator. By not having an iron core, the iron core losses can be

reduced using slotless stator or eliminated by the use coreless stator. This approach is especially useful for high-speed machines, where core losses can impact total motor efficiency [8] and reduced cogging torque improves machine smoothness. Also, elimination of stator core can result in overall lower machine weight. The downside of slotless and coreless stators comes from the reduced stator linkage and in turn lower torque output.

Both slotless and coreless BLDC machines can be considered to have an air core, where the ideal back-EMF has a clean sinusoidal shape. Clean sinusoidal back-EMF persists even at high rotational speeds, due to lack of iron core and respective core saturation effects. This feature results in machine smooth running at high speeds, but only if sinusoidal commutation or FOC is used. Trapezoidal commutation won't match the back-EMF shape and result in lower efficiency [11] and increased acoustic noise [4].

1.3 BLDC machine control approach

In addition to the trapezoidal and sinusoidal commutation mentioned earlier, there also exists an advanced control algorithm called Field-Oriented Control (FOC). By using stator current, rotor position and transformations, it is possible to achieve low torque ripple, best dynamic response, generate full torque across whole speed range and achieve higher efficiency than two methods mentioned above. All these benefits come at increased computational cost and algorithm complexity. [17]

1.3.1 Trapezoidal commutation

The simplest BLDC commutation approach is a trapezoidal commutation (also known as 6-step or 120^{0} commutation). By following switching order shown in Figure 1.3, a modified sine waveform creates a rotating magnetic field, which in turn generates torque in the rotor. The elegance on this approach is that just as torque from one phase starts to decline, it is possible to switch to another phase that is on upswing [18].

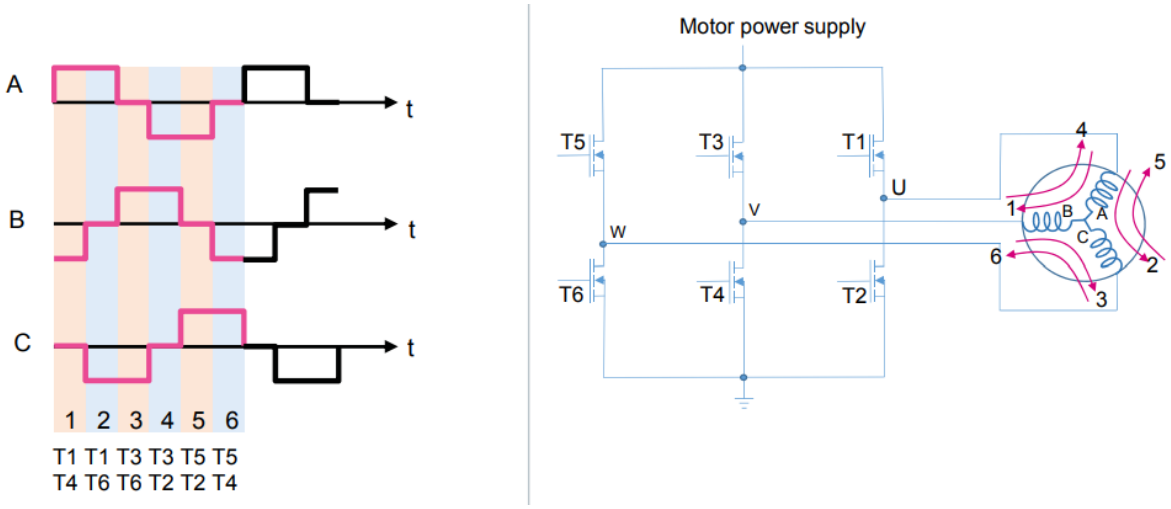

Figure 1.3 Trapezoidal commutation visualisation [19]

One of the differentiating features of trapezoidal commutation between the other commutation types comes from the fact that only two motor windings carry current at any given time (see Figure 1.3) [3]. But consequently, a significant amount of current ripple is generated in the BLDC. This non-linearity creates noise and vibrations in the motor, whose acceptability depends on the application.

If the peak torque generated by machine is normalized to 1, then minimum torque is 0,866 (sine of 60⁰). From this comes statement, that BLDCs have large torque ripple (13% peak to peak) [18]. Although the torque ripple might be large, it is acceptable in certain applications (especially in low-end applications [12]) and is significantly less noticeable at higher rotation speeds due to BLDC mechanical inertia and other connected parts. By applying a PWM signal during the switch conduction time, it is simple to achieve fine control over the speed of the BLDC.

The main challenge with trapezoidal approach is correctly timing the commutation, for which there are two widely adopted approaches: sensored and sensorless.

Sensored approach traditionally uses three hall sensors to determine the approximate rotor position based on existing lookup table. The three hall sensor lookup table provides rotor position feedback with 60⁰ accuracy and although position accuracy is quite poor, it is good enough for 6-step commutation [18]. Higher accuracy rotor position sensors like resolvers can be applied for improved machine performance but are not strictly necessary.

Sensorless approach gets rid of the position sensors and instead uses the BLDC back-EMF zero crossings to time the commutation (see Figure 1.4). As explained earlier, only two motor windings carry current at any given time. Trapezoidal commutation exploits this feature and forces zero current twice in each phase during six step period and by

using the third floating phase, the back-EMF can be directly measured by the ADC of the MCU [20]. This gives possibility to create cheap and simple closed-loop operation without any external position sensors.

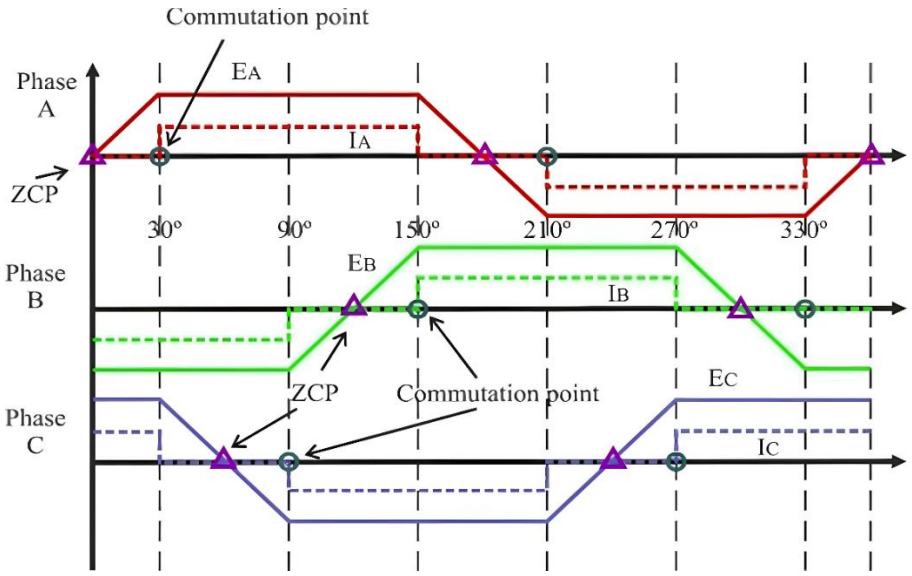

Figure 1.4 Sensorless 6-step commutation timing based on BLDC back-EMF [21]

Machine sensorless startup is a challenge, as back-EMF depends directly on the speed of the rotor and there won't be reliable back-EMF signal at low speeds. As common workaround, BLDC is first aligned and started in open-loop ramp-up mode (see Figure 1.5). Rotor is blindly aligned by supplying current to one of the phases and after some predetermined delay, ESC applies a ramping open-loop rotating waveform. After sufficient speed is achieved, closed loop control is enabled using the back-EMF [18]. This approach is widely used in UAV applications, where motors have low load at low RPM and won't encounter cogging issues during startup.

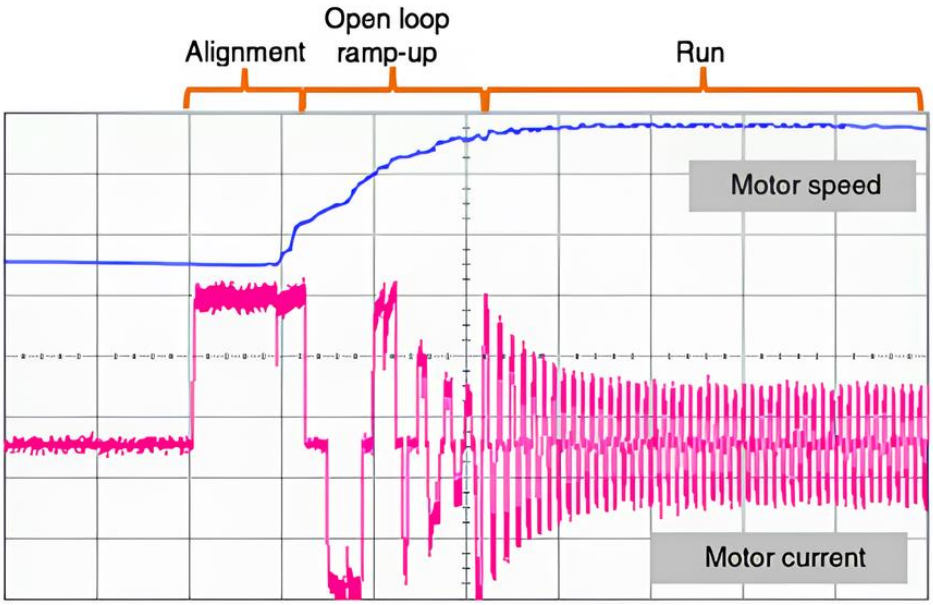

Figure 1.5 Sensorless BLDC startup procedure [18]

1.3.2 Sinusoidal commutation

The sinusoidal commutation replaces the flat peaks of the trapezoid with a sinusoidal waveform on all three phases of the BLDC. To achieve three phase sinusoidal waveform, it is necessary to overlap the commutation of phases, selectively firing more than one pair of power switching devices at a time [12].

Both open- and closed-loop control is possible with this commutation, but requires an accurate speed or position feedback sensor for smooth operation. Sinusoidal commutation is typically used in midrange performance applications requiring smooth speed and torque control [12].

To generate the output waveform, sinusoid waveform is quantized, and a simple lookup table is created with angle and corresponding PWM value (see Figure 1.6). For more finer control, the sine-modulated PWM can be multiplied by any factor between zero and one to achieve lower output voltage. By supplying clean sine wave, in addition to lower noise, it eliminates the torque ripple and non-linearities in motor current, which occur inherently with the six-step commutation [12].

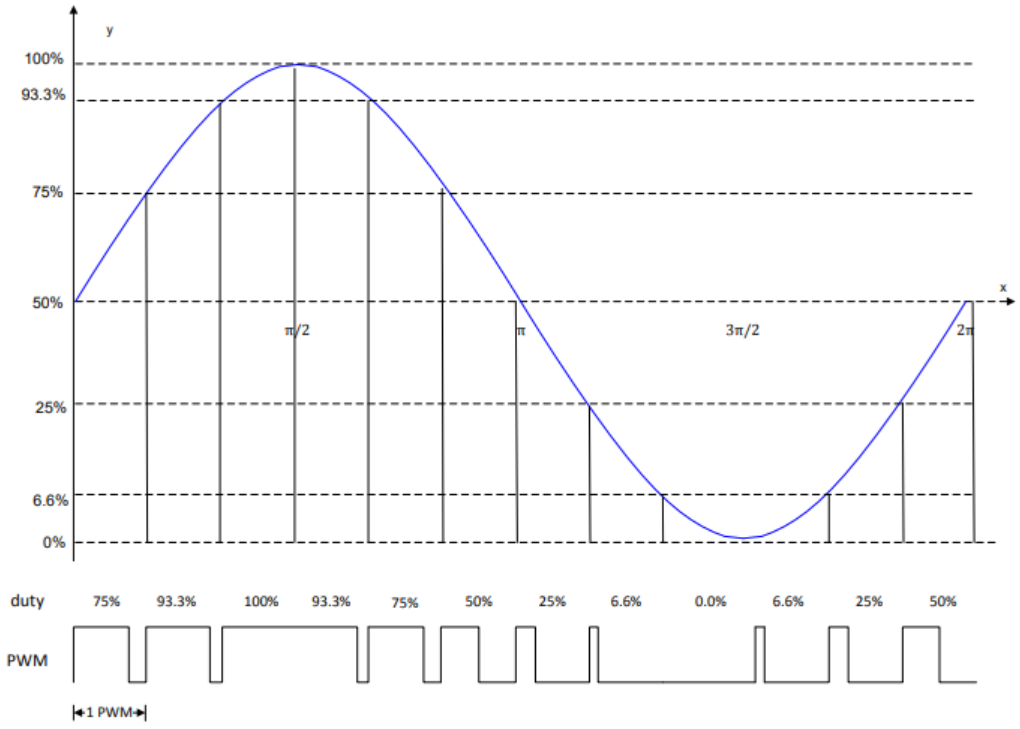

Figure 1.6 12 sample point Sine Wave with Corresponding Modulated PWM [22]

Sinusoidal commutation requires higher resolution position feedback devices, more computation and incurs additional switching losses. This makes the sinusoidal commutation more expensive than the six-step commutation, but provides reduced torque ripple and allows for more precise control [12].

1.3.3 Space Vector Modulation and third harmonic injection

Space Vector Modulation is a more modern technique used in many Variable Speed Drives (VSD) today. Using standard sinusoidal PWM on a three-phase inverter, the required voltage for each leg of the inverter must be calculated separately and modulated on top of a PWM carrier. However, Space Vector Modulation significantly simplifies process as with this technique, the entire inverter is treated as a state machine having six binary inputs and three binary outputs. [23]

Six binary inputs results in 64 possible inverter states [23]. Most of them are discarded as they result in catastrophic situations happening to the inverter (such as switching a top and bottom transistor on at the same time). In total there are eight useful states (see v_0 – v_7 on Figure 1.7). Six of these states result in voltages being applied to the machine windings and two states result in zero voltage on the motor windings (the zero vectors).

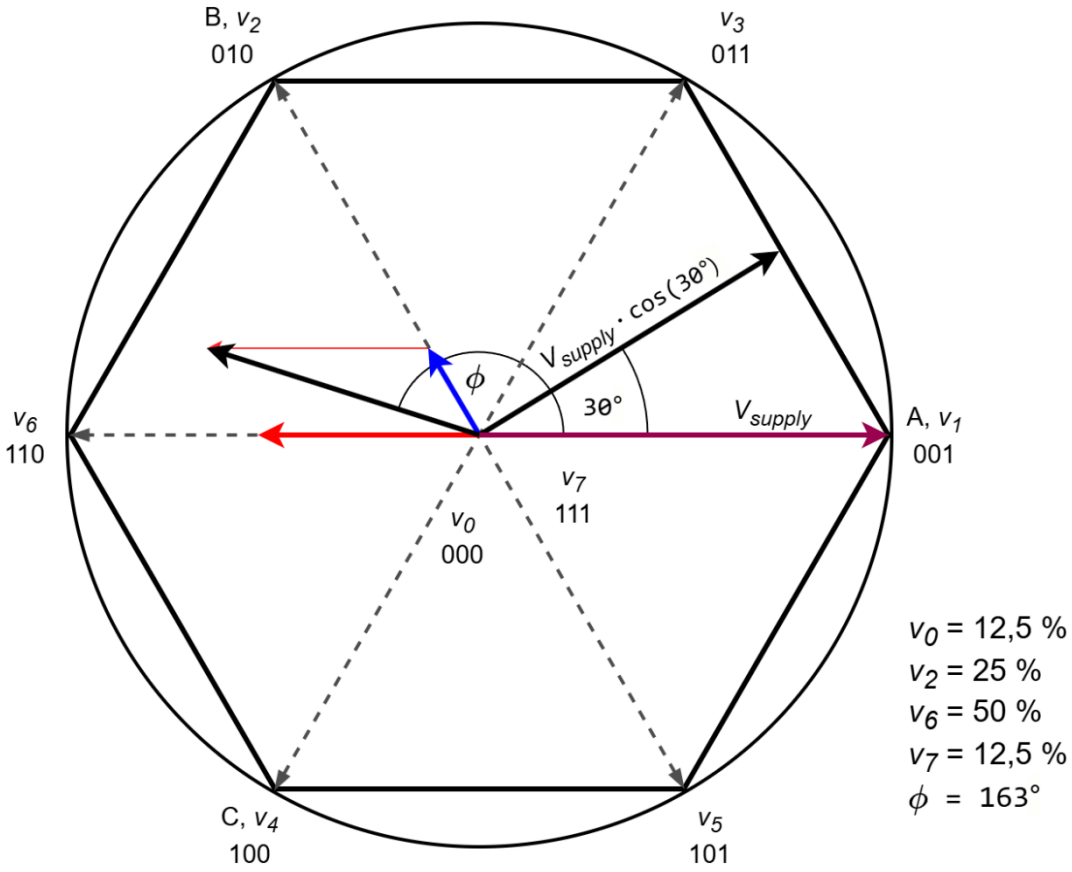

Figure 1.7 On this figure, eight basic SVM vectors v_0 – v_7 with their magnitude and direction can be observed, including two zero vectors v_0 and v_7 shown at origin point. 163º voltage reference at 71 % of V_{supply} was achieved by combination of the basic vectors v_2, v_6 and zero vectors. Hexagon shows the maximum inverter output voltage achievable for all angles without use of overmodulation. If third harmonic injection is applied (1,15 modulation factor), then circle illustrates maximum inverter output voltage. [24]

If the resulting voltage states on a space vector diagram are overlaid on a motor, it shows not only the amplitude of each voltage state, but its direction as well (see 163º voltage reference example on Figure 1.7). These vectors show the direction that the inverter will attempt to establish a magnetic field on the motor for that state [23]. To achieve rotating voltage vector, inverter jumps from one state to the next. Those jumps are rather sharp and will result in rough rotor movement, as this kind of commutation is in its essence trapezoidal commutation explained previously.

To achieve smoothly rotating voltage vector, the voltage vector must be capable establishing at any angle. This can be achieved by quickly switching between two adjacent voltage vectors and by exploiting the inductance of the motor, as it will average the effect and make the resulting vector somewhere in-between the two vectors. [23]

As can be seen from Figure 1.7 an arbitrary voltage vector at 163º and 71 % magnitude was achieved by switching back and forth between states v_2, v_6 and zero vectors. Resulting vector angle can be changed by spending different amount of time in each of the base vectors and magnitude by increasing or reducing the ratio of the zero vectors (See Equation 1.1). When the desired angle exceeds the bounds of one of the sectors, switching strategy must choose appropriate vectors to switch between. This way a voltage vector can be created at any given angle or magnitude and smoothly rotated across all sectors.

$$\begin{cases} T_1 = T \cdot m \cdot \sin(60 - \theta) \\ T_2 = T \cdot m \cdot \sin(\theta) \\ T_0 = T - T_1 - T_2 \end{cases} \quad (1.1)$$

where T_1- active time for first vector, s,

T_2- active time for second vector, s,

m – modulation factor,

T_0- active time for zero vectors, s,

θ – voltage reference vector angle, rad,

T- total switching period, s.

One side-effect of the SVM is that only base vectors can utilize full input supply voltage, and maximum inverter output voltage follows Equation 1.2 [24] for in-between base vectors. This comes from the fact that some of the voltage is lost when switching between the base vectors (see Figure 1.7) and requires additional techniques like third harmonic injection to compensate for the lost supply voltage.

$$V_{max,RMS} = V_{Supply} \cdot \cos\theta \tag{1.2}$$

where $V_{max,RMS}$ – Maximum inverter output voltage, V,

V_{supply} – Inverter supply voltage, V,

θ – voltage reference vector angle, rad.

Third harmonic Injection (see Figure 1.8) is one of the widely used patterns achieved by re-ordering the switching states within a switching period using SVM [24].

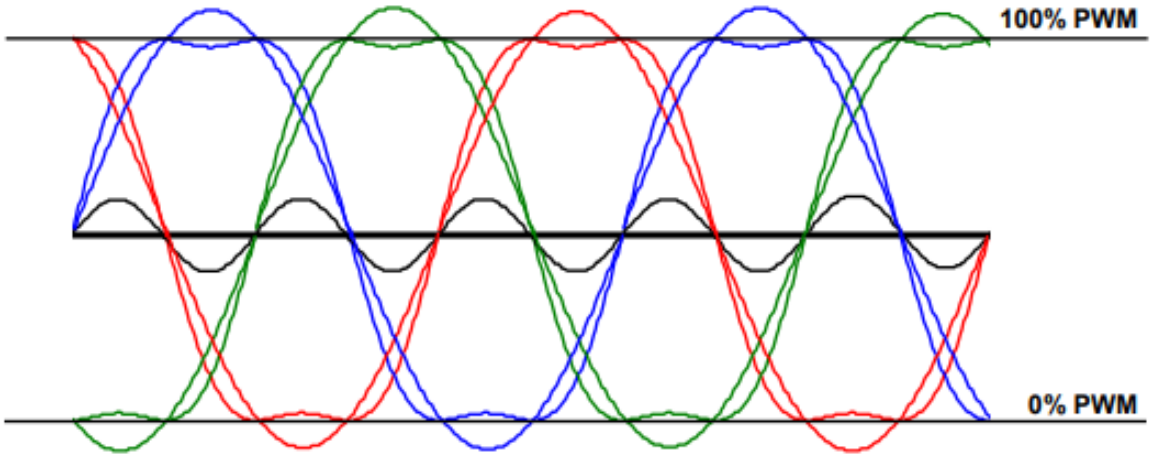

Figure 1.8 Space Vector modulation with third harmonic injection [23]

When a small third harmonic is intentionally injected to the sinusoidal signal, it ends up distorting the clean sine waveform. By distorting the waveform, it enables the inverter to use supply voltage more effectively and supply BLDC with 15 % higher phase voltage by exploiting the neutral point common mode voltage oscillations. Although supply voltage stayed the same, phase to neutral voltage increased. The factor by which the effective machine voltage is increased is called modulation factor. The BLDC phase to phase output voltage follows equation 1.3 [24]:

$$V_{max,RMS} = \frac{V_{Supply}}{2} \cdot \sqrt{3} \cdot \frac{1}{\sqrt{2}} \cdot m \tag{1.3}$$

where V_{supply} – Power stage supply voltage, V.

Using third harmonic injection, a clean waveform will be generated up to modulation factor of 1,15 [24]. If the modulation factor is increased even more, the sine wave is distorted more and more by higher frequency harmonics until the output waveform reassembles closely trapezoidal shape and effectively boils down to 6 step commutation explained previously. Maximum modulation factor doesn't generally exceed 1,15, performance gain above this modulation factor are not worth increased power consumption and vibrations.

1.3.4 Field Oriented Control

Field Oriented Control (FOC) also known as Vector Control, is a control method in which three-phase stator currents and rotor position are measured and transformed into a flux generating and a torque generating component (see Figure 1.9) [12]. The FOC is mainly suitable for the high-end applications due to its complex design and higher processing requirements. FOC maintains high efficiency over a wide operating range and provides superior dynamic response. [12]

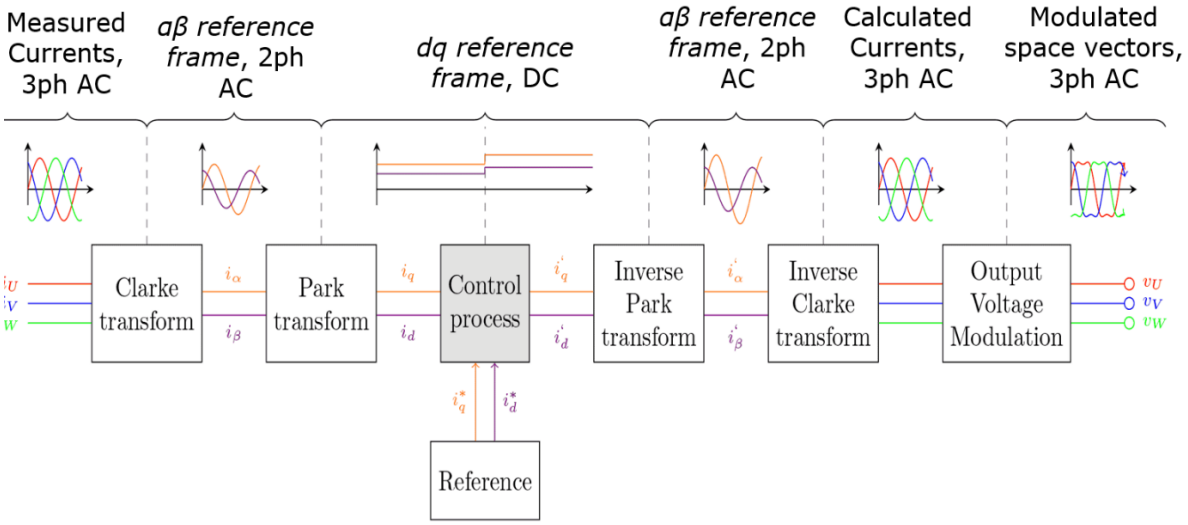

Figure 1.9 Field Oriented Control workflow [24]

FOC workflow relies largely in Clarke and Park transformations to get flux and torque components. First the Clarke transformation converts phase currents from the three-phase sinusoidal system (A, B, C) into a two-phase time variant system (*αβ*, see Equation 1.4). In this system, two *αβ* phases are at 90⁰ offset between each other and in their essence are active and reactive current components of a three-phase system. As implementing PID controller in time variant system is inconvenient, the Park transformation is applied to obtain two-coordinate time invariant system (*dq*, see Equation 1.5).

In literature, the motor flux generating component is commonly called direct (*d*) and a torque generating component quadrature (*q*). As the *dq* system is time invariant, it gives ability to use simple PID controllers to keep the measured current components at their reference values.

$$\begin{cases} \begin{bmatrix} i_\alpha \\ i_\beta \end{bmatrix} = \begin{bmatrix} 1 & 0 \\ \frac{1}{\sqrt{3}} & \frac{2}{\sqrt{3}} \end{bmatrix} \begin{bmatrix} i_a \\ i_b \end{bmatrix} \\ i_a + i_b + i_c = 0 \end{cases} \quad (1.4)$$

where i_a, i_b and i_c - three-phase components in the *abc* reference frame, A,

i_α and i_β - two-phase orthogonal components in the stationary *aβ* reference frame, A.

$$\begin{bmatrix} i_d \\ i_q \end{bmatrix} = \begin{bmatrix} \cos\theta & \sin\theta \\ -\sin\theta & \cos\theta \end{bmatrix} \begin{bmatrix} i_\alpha \\ i_\beta \end{bmatrix} \quad (1.5)$$

where i_d and i_q - direct and quadrature axis orthogonal components in the rotating *dq* reference frame, A,

θ – angle offset between i_α and i_d, rad.

After PID controller has made necessary control actions, next step is to convert the *d* and *q* values back to three phase sinusoidal system. First inverse Park transform (see Equation 1.6) is applied to get *aβ* system, after which either inverse Clarke's transform (see Equation 1.7) is used with sinusoidal commutation or Space Vector Modulation directly applied on αβ system to get modulated output waveform (see Figure 1.9).

$$\begin{bmatrix} i_\alpha \\ i_\beta \end{bmatrix} = \begin{bmatrix} \cos\theta & -\sin\theta \\ \sin\theta & \cos\theta \end{bmatrix} \begin{bmatrix} i_d \\ i_q \end{bmatrix} \quad (1.6)$$

$$\begin{bmatrix} i_a \\ i_b \\ i_c \end{bmatrix} = \begin{bmatrix} 1 & 0 \\ -\frac{1}{2} & \frac{\sqrt{3}}{2} \\ -\frac{1}{2} & \frac{\sqrt{3}}{2} \end{bmatrix} \begin{bmatrix} i_\alpha \\ i_\beta \end{bmatrix} \quad (1.7)$$

As can be seen from Equation 1.6 and 1.7, high processing power requirement comes from the fact that every FOC control loop iteration, multiple trigonometric functions must be executed. Typically, maximum speed achievable by FOC is often limited by available computational power, but in some cases BLDC machine maximum speed is achieved first. Nevertheless, maximum achievable FOC electrical speed is typically lower than trapezoidal or sinusoidal commutation due to increased overhead.

As can be seen from both Park transformations, for FOC to work well, both BLDC phase currents and accurate rotor angle must be known. BLDC phase currents must be

measured on at least 2 phases, as in balanced three phase system third phase can be derived from relationship $i_a + i_b + i_c = 0$. Without current measurement, field strength cannot be measured and in turn hard to achieve good control [25]. As a fallback, FOC can be done by controlling phase voltages instead of current, but it is not true FOC and won't give equal performance the method mentioned before [25].

Rotor angle estimation In addition to current sensors, accurate rotor angle estimation is important to make accurate Park transform and in turn, achieve high FOC performance. So similarly to 6 step commutation, two approaches exist: Sensored and Sensorless.

Sensored approach did not have many changes compared to 6-step commutation. Main change comes from higher quality of sensor requirement, as the better the rotor position estimation, the more accurate Park transform and in turn FOC performance. Although FOC can be done using three hall sensors by additionally applying sensor smoothing algorithm, its performance is not comparable to that of the dedicated high-speed rotatory encoders sensors, for example: AS5600, MT6816 and many other sensors.

Sensorless approach has multiple new angle estimations techniques available as FOC requires access to the phase currents. Some of the techniques are Flux Observer, High Frequency Injection and other model-based approaches [26]. A general block diagram example of sensorless FOC can be seen on Figure 1.10. Figure 1.10 Block diagram is overall very similar to the Figure 1.9, main difference is an additional block for Position and speed estimation.

As techniques mentioned earlier have high complexity and are not the focus of current thesis, the explanation of the working principle is not in the scope of the thesis.

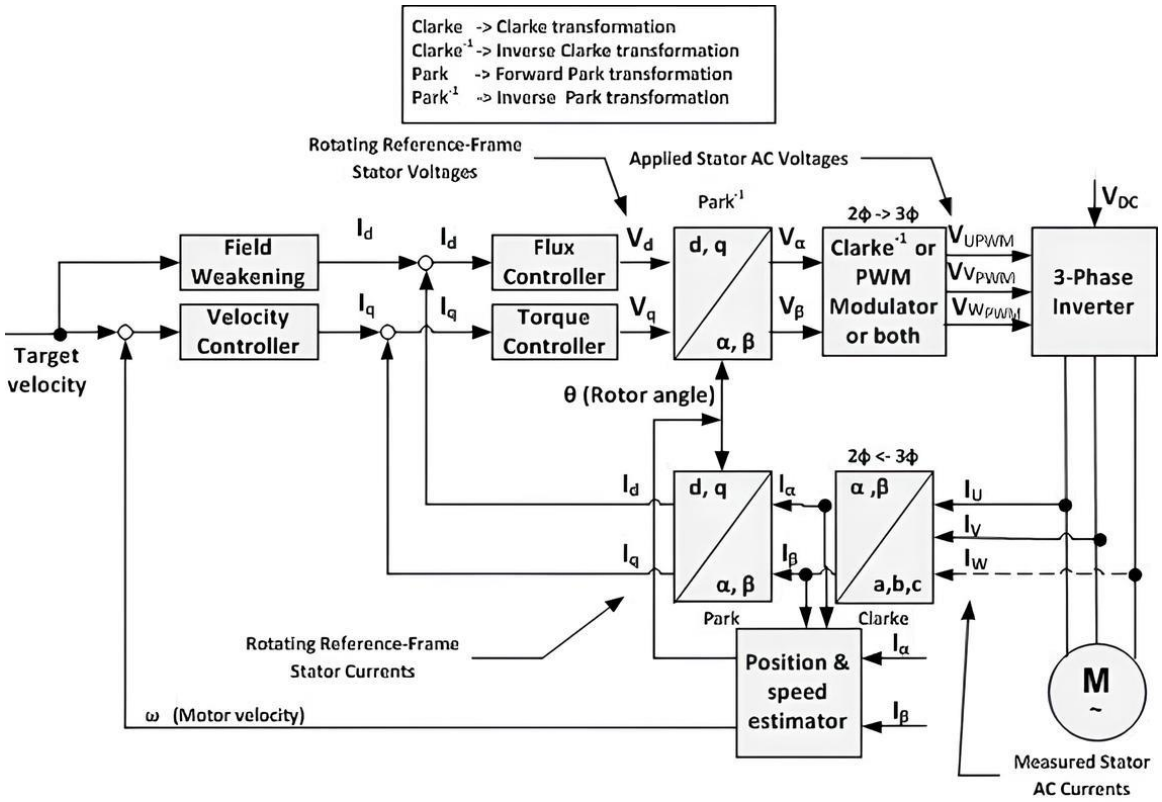

Figure 1.10 Block diagram for sensorless FOC [27]

FOC advantages are illustrated well on Figure 1.11, where sinusoidal control offers similar performance at low speeds. As the speed increases using sinusoidal control, the *d*-axis current rapidly increases while *q*-axis current stays about same across whole speed range. With FOC *d*-axis current can be regulated to stay at 0 A, which achieves significantly lower losses in stator at similar speeds.

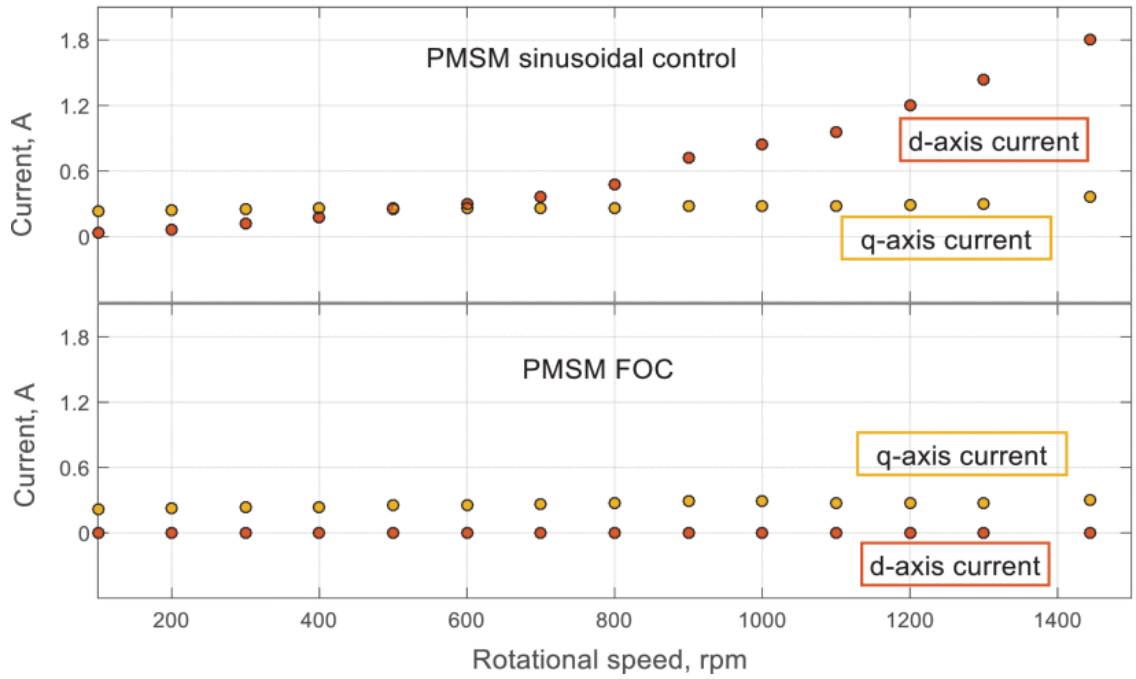

Figure 1.11 Current requirement comparison between sinusoidal control [28]

By going through the complexity of FOC algorithm, multiple advantages are achieved. As the torque and flux component values are known, it is possible control *dq* currents and operate in the maximum torque per amp (MTPA) region [29]. This achieves lowest losses in the stator as the highest torque density is achieved and overall efficiency is improved.

1.3.5 Control approach summary

There are multiple approaches to control BLDC machines, where each approach has advantages and disadvantages. Table 1.2 shows short summary between different commutation approaches. If the best performance is desired and enough computational power is available, then FOC approach is clear choice as best machine control approach.

Table 1.2 Commutation approach comparison [12] [17]

Commutation approach	**Trapezoidal**	**Sinusoidal**	**FOC**
Dynamic response	Good	Good	Best
Torque control at Low Speed	Large Torque Ripple	Excellent	Excellent
Torque control at High Speed	Good	Inefficient	Best
Minimum Feedback Device	Position sensor: Hall sensors or better	Position sensor: Encoder or Resolver	Current Sensor and Position sensor: Encoder, resolver or model based
Algorithm complexity	Low	Medium	High

1.4 Electronic Speed controller

Electronic Speed Controller (ESC) is typically a 3-phase inverter power stage with accompanying microprocessor, position feedback circuit and control input (see Figure 1.12). ESC in their principle can be considered similar to the Variable Speed Drives (VSD) used in industrial applications, but with few differences. The vast majority of ESC-s are designed to work with PMSMs and BLDCs using DC source, while VSDs can additionally accept induction machines and work with AC sources.

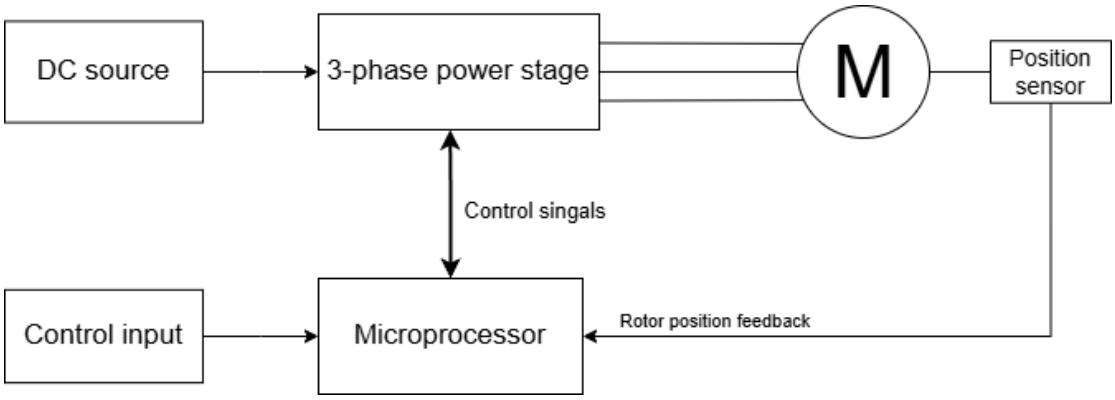

Figure 1.12 Simplified classical ESC diagram

The 3-phase inverter circuit can be seen on Figure 1.13. For every phase, a half-bridge circuit is needed, so for 3-phase machines at least 6 switches are needed with appropriate gate drivers. Depending on the rated voltage of inverter, both IGBT and MOSFET switches can be used, but at voltages below 300 V are predominantly dominated by MOSFETs due to significant lower losses compared to IGBT solutions. As this thesis is focused on low voltage UAV applications, IGBTs won't be discussed.

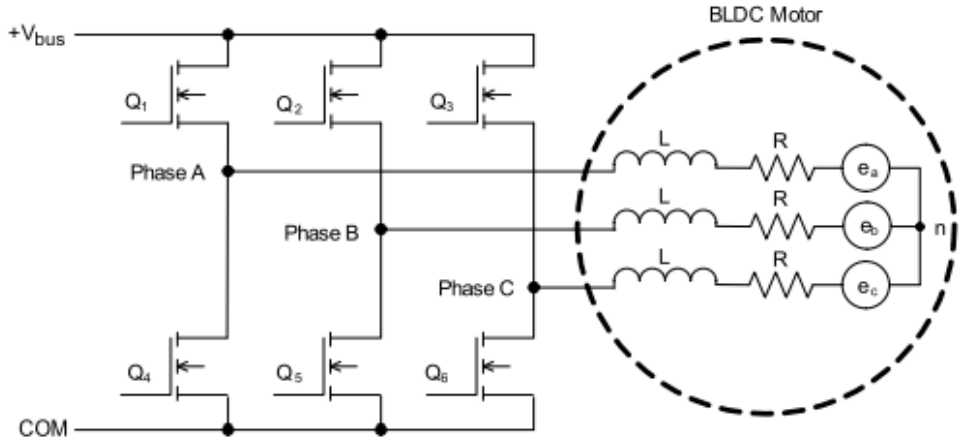

Figure 1.13 3-phase inverter circuit [12]

The heart of the ESC is the microprocessor (MCU). Its task is to interpret control input, gather rotor position feedback, generate PWM signals for the 6 switches based on chosen commutation and control input. ESC protections (overcurrent, overtemperature, over and undervoltage) are also handled by MCU. If ESC uses FOC, then Clark and Park transformations are also handled by microprocessor.

Significant difference between ESC and VSDs can be found in the control loops. VFDs can control directly the output frequency (open or closed loop) or torque of the electrical machine. Whereas the affordable ESCs commonly only commutate the BLDC motor in accordance with the control input without tightly regulating the output speed or torque. This approach is acceptable if tight regulation or linear response is not needed like in

UAV applications. If ESC with tighter control or programmability is required, multiple solutions are available on market, but at increased cost. Nevertheless, with additional hardware and software, ESCs can achieve function parity with VSDs. ESCs can typically drive machines at significantly faster speeds than VSDs, upwards of 200000 electrical rpm (3333 Hz) can be achieved.

Commercially available ESCs are primarily designed to work with low voltage DC sources like batteries or other DC supplies typically below 60 V. ESCs are very widespread in Unmanned Vehicles (UV) and Robotics, due to their small size, high power density and ability to work without a grid connection.

1.5 Existing ESC solutions

A wide variety of different ESC solutions already exists on the market for different applications. As the number of the existing solutions is enormous, the market can be split in multiple diverse ways, so author proposed two following classifications: ESC Degree of Openness and current capability.

1.5.1 ESC classification by Degree of Openness

ESC Degree of Openness can be divided into three distinct categories:

1. Proprietary hardware and software
2. Proprietary hardware, but open-source software
3. Open-source software and hardware

The vast majority of the ESCs available on the market are the proprietary type, with both hardware and software not publicly available. As companies are using their products to make profit and ESC market has many competitors, it is financially disadvantageous to share their development with 3rd parties. Notable examples from this category include newer Odrive and BLHeli_32 based ESCs.

A popular approach has been open-source release of the software under MIT or GNU General Public License (GPL), while keeping the hardware proprietary. This way community can work on and improve the software side, while making it nontrivial for competitors to clone the hardware. Notable examples include older Odrive ESCs, newer VESC ESCs, BLHeli_S ESCs and other UAV ESCs. Under this category are also included open-source software projects, that were created by community as replacement for

proprietary software like AM32 project, which was open-source alternative to the BLHeli_32 proprietary software.

Third and the least widespread category is the open-source category. In this category many smaller individual, specialized projects and non-profit oriented products can be found. As making a profit is not priority, this gives creators option publish all files for free for everyone to use. Notable examples include SimpleFOC ESCs, BlueESC and other individual projects (Dagor, FOCn).

1.5.2 ESC classification by current capability

Second way to divide the commercially available ESC is by the phase current capability. Following categories are proposed:

1. Low current applications
2. Medium current applications
3. High current applications

First category features ESCs and driver circuits with phase current below 5 A and/or maximum input voltage of 25,6 V (equivalent to 6 series connected lithium polymer battery cells, 6S LiPo). These ESCs are meant to drive high stator resistance motors like cooling fans, gimbal motors, miniature unmanned vehicle (UV) motors and other motors used in low power applications. ESC prices in this range are low, typically below 40 €. As the currents are not very high, single IC motor drive solutions are available on the market like DRV8316 and L6235 that have all 6 switches and gate drivers integrated inside.

Second category has ESCs with phase current rating below 80 A and maximum input voltage of 52 V (equivalent to 12S LiPo battery). Typical applications at this current ranges feature small to medium sized UVs, E-bike, E-scooters. Due to significant increase in current and in turn heat density, large discrete switches and other components must be used, which significantly increases size, weight and ESCs cost. ESC in this range cost typically below 200 €.

ESCs in third category feature phase currents over 80 A and input voltages above 52 V. At these high of current and power range, single discrete switching components typically can’t handle such high losses and multiple are placed in parallel to achieve higher performance. Additional heatsinks, cooling fans and water cooling are employed to keep components from overheating. Applications include large UVs and powering of traction motors. In the lower end of this category, prices are in hundreds of euros but can reach thousands of euros in case of traction motors in electrical vehicles and buses.

2 ESC PROTOTYPE DESIGN

As this thesis is focused on coreless machines, which back-EMF shape is almost pure sinusoidal, use of commercially available ESCs is suboptimal as majority of ESCs use 6-step commutation. Due to points highlighted in literature review, author decided to design and prototype ESC with ability to use FOC.

First potential use cases are looked over and list of specifications is compiled. Then based on the specification, a solution is proposed that meets as many specifications as possible. Before detailed design of printed circuit board (PCB) is started, a MATLAB Simulink simulation is performed followed by set of thermal calculations to ensure specifications can be met and component maximum ratings are not exceeded

2.1 Proposed solution

Before design process can proceed, proposed solution using a system diagram needs to be compiled (see Figure 2.1). On system diagram simple overview of all used features and connection points is done. Figure 1.12 is taken as base and modified to satisfy specifications from Table 2.1. System diagram is important to get as close as possible to final solution, as mistakes and oversights missed during this stage will result in additional time and cost during later design phases or outright failing to meet specification.

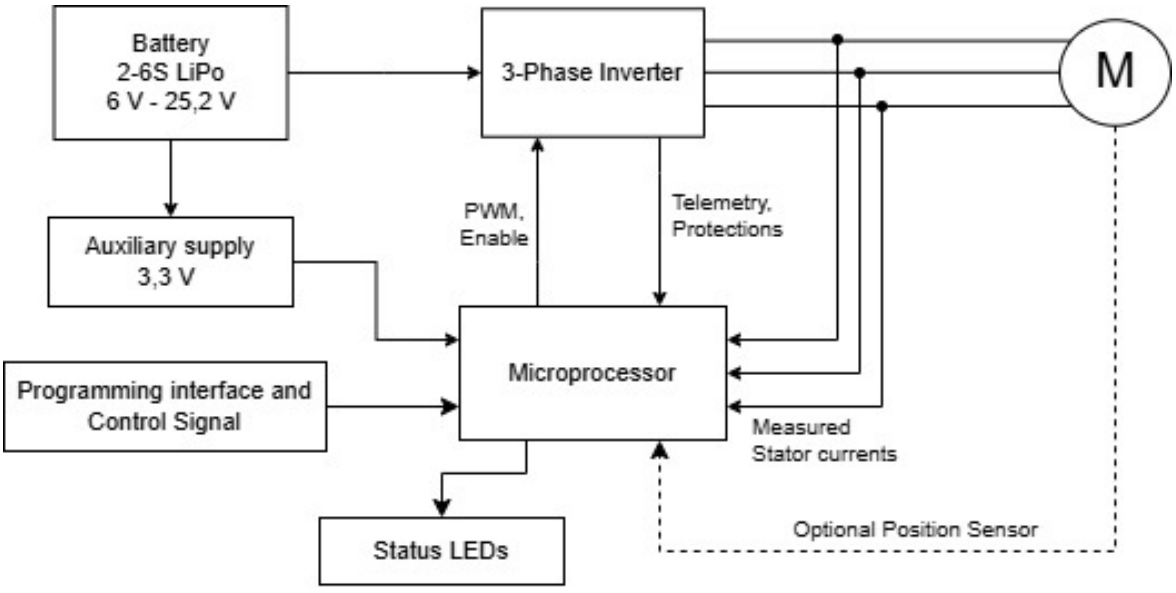

Figure 2.1 ESC proposed solution system diagram

From Figure 2.1 can be seen, that there are three additional parts in the proposed solution compared to the Figure 1.12. These are 3,3 V auxiliary supply, programming interface and status LEDs.

Voltage supplied by the battery is too high to directly connect to the MCU, so a buck converter is used to convert battery voltage to voltage acceptable by the MCU. Exact working voltage depends on the MCU, but most modern MCUs accept 3 – 3,6 V as the working voltage. In addition, the DC/DC converter must be designed to be able to handle enough current to power the MCU across input voltage range.

Programming interface is interface through which firmware is uploaded to the MCU. There is no universal programming interface, it depends on type and manufacturer of MCU. In a mass production product, the programming interface doesn't have to be easily accessible, as firmware is uploaded once at the factory. This is not the case with prototypes, where firmware can change often and easy access to the programming interface is critical.

Status LEDs do not directly affect the performance of ESC but are in place for the user. LEDs are good at conveying user the status of ESC without the need for a wired connection. A single LED can be used by encoding status with certain blinking patterns, but RGB LED offers a more user-friendly approach if board space and cost is not critical. For example, green LED can indicate normal operation, red LED a fault and blue loss of control signal.

2.2 Prototype ESC specifications

As was explained in the previous chapters, coreless machines could be used in many applications, but one of potential application is in the UAVs. Propellers need high rotational speeds to generate meaningful amount of lift, so high-speed coreless machine could fit very well into this application.

Next, size class of the UAV needs to be decided, as this will determine required lift and in turn motor size and ESC current capability. To simplify the design process and use already widespread category on the market, a sub 250 g multirotor category was chosen. This category has a lot of off existing designs that can be used as reference and as phase currents are low, the ESC can be made at a reasonable cost and at relativity low complexity.

Although many UAVs in sub 250g category are meant to be powered by 2S or 3S LiPo batteries, this low of a voltage might pose problems to the coreless machines. The lack of iron core results in lower stator flux and in turn lower torque output. To compensate, larger PM, increased PM pole count or more stator turns can be employed. This in turn reduces the machine k_V rating or the maximum rotational speed of the machine, but higher battery voltage can compensate for that. To keep the ESC flexible, input voltage range is increased to support 6S LiPo batteries (Maximum 25,2 V).

The sub 250 g category is quite limited in size and weight, so ESC size and weight should be minimized. Low weight also has benefit of not requiring large power from the motors. This enables use of ESCs in the low current applications category. So, ESC needs to be able to handle at least 5 A of phase current.

As discussed earlier, matching back-EMF shape of the machine is important to achieve highest efficiency and low acoustic noise. Due to this point, either sinusoidal commutation or FOC must be used. As UAVs typically employ sensorless approach for the commutation, ESC designed by author must also support sensorless commutation. To keep ESC flexible, sensored backup option should be also implemented.

All points gathered from earlier are compiled into table of specifications found in Table 2.1.

Table 2.1 ESC Specification table

Input voltage	6 V – 25.2 V (2S-6S LiPo)
Phase current capability	at least 5 A
Commutation	FOC
Sensor support	Hall sensors, rotary encoder
Protection features	Overvoltage, overcurrent, undervoltage, overtemperature

In addition to the prototype ESC Specification, parameters of the prototype coreless machine (see Figure 2.2) used in this thesis are provided in the Table 2.2.

Table 2.2 Prototype coreless machine parameters

Phase resistance	5,95 Ω
Phase inductance	0,302 mH
Rotor pole pair count	1
Estimated Flux linkage	0,03 Wb
Stator wiring	Wye configuration

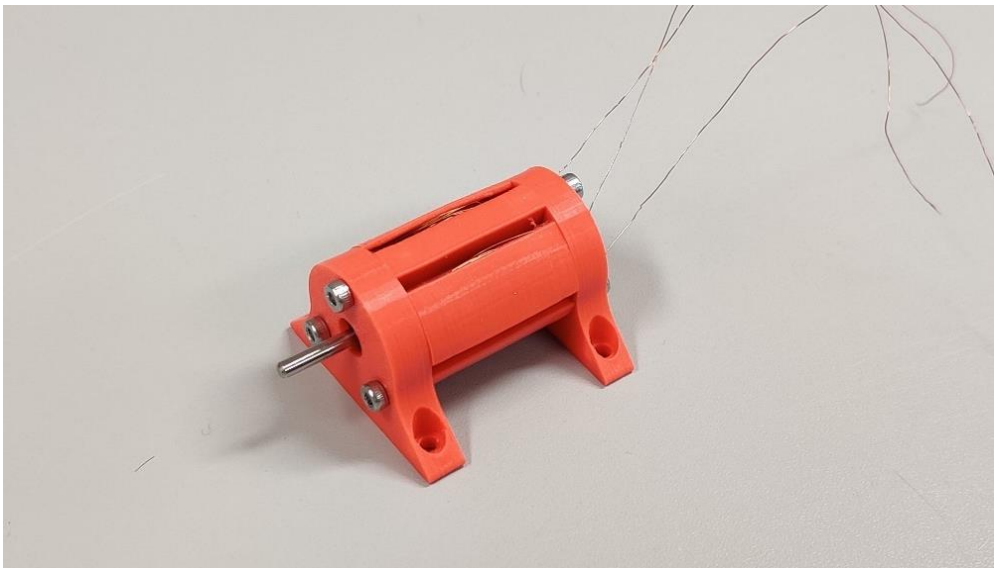

Figure 2.2 Prototype coreless machine used in thesis

2.3 Component selection

This section explains more thoroughly choice of each individual component and different consideration taken to meet the specifications. While all parts shown in Figure 2.1 are important for the operation of the ESC, two by far the most important components are microcontroller and 3-phase inverter. Both must be chosen carefully with enough safety margin to stay within specification to avoid a catastrophic failure.

2.3.1 Microprocessor

As explained earlier, the most important part of the ESC is the Microprocessor. All individual ESC parts are connected and handled by MCU, so it needs to have wide array of peripherals like fast ADC, high speed hardware PWM, and enough of general-purpose input-output (GPIO) pins to handle all auxiliary connections.

Additional requirement for the MCU is high computational power, due to large number of calculations needed for FOC, which can be achieved either by a powerful single core or a dual core MCU.

As requirements above are still too broad, the MCU selection is narrowed down by using data provided by the open-source FOC software library SimpleFOC [25]. The two MCU families with highest performance were from ESP32 and STM32F4 families. To decide the best MCU family, comparison is compiled in Table 2.3. Exact models for comparison are ESP32-S3 Mini (smallest module size) and STM32F405 (best overall compromise).

Table 2.3 Comparison between ESP32S3 and STM32F4 MCU

	ESP32-S3 Mini	**STM32F405**
Coremark score	1182	608
Core count	2 cores	1 core
GPIO count	39	51
ADC and channel count, sample rate	2x 12-bit ADC 20 channels, 0,1 Msps	3x 12-bit ADC 24 channels, 2,4 Msps
Price (1 pc)	2,95 €	11,11 €

Data from Table 2.3 unfortunately doesn't provide clear choice, and compromise must be made. The ESP32-S3 offers higher computational performance and ability to split workload between two cores. STM32F405 offers higher GPIO count and significantly higher ADC performance but at almost four times higher cost.

MCU chosen by author is **ESP32-S3 Mini**, due to higher computational performance and significantly lower cost. While low ADC sample rate could limit maximum speed and PWM frequency due to requiring phase current measurements, even at rotational speeds of 200000 electrical rpm (3333 Hz), the MCU will have more than enough sample rate for smooth operation.

2.3.2 3-Phase inverter

Second important component of the ESC is the 3-phase inverter circuit with its gate drivers and switches. As phase current specification is quite low, it offers two approaches: single fully integrated motor driver IC or discrete MOSFET and gate driver combination.

To meeting phase current measurement requirement, the driver IC or gate driver must support phase current measurement as sensorless FOC is not possible otherwise. Current measurement hardware integrated into IC is preferred due to smaller overall size offered by component integration.

Due to high current requirement, only one integrated motor driver IC is available on the market that meets both voltage and current requirements: Texas Instruments DRV8316C motor driver IC. It can handle 8 A peak phase current, accepts 4,5 V – 35 V, includes all protections required by specification and has integrated shunt-free current sensing. It also has SPI interface for advanced diagnostics and IC configuration.

As opposed to the integrated motor driver ICs, second approach has more options available on the market as gate driver and MOSFETs are in separate packages. This

results in significantly higher phase current capabilities due to larger surface area for heat dissipation and lower conduction losses offered by discrete components, but at the downside of increased size of inverter. Shunt-less current sensing is also not possible due to no control over the MOSFETs used in the inverter. As example, DRV8305 smart gate driver is used.

Table 2.4 Comparison between DRV8316C Integrated Motor Driver IC and DRV8305N discrete MOSFET and gate driver solution

	DRV8316C	**DRV8305N**
Peak phase current	8 A	MOSFET dependent
Total solution PCB area	Small	Large
PCB routing complexity	Low	High
Shunt-less phase current measurement	Yes	No
Price (1 pc)	4,66 €	3,88 €, MOSFETS not included

Due to lower PCB size offered by integrated IC and shunt-less current measurement, author chose **DRV8316C** IC for the 3-phase inverter circuit. While operation at high phase currents will result in larger losses in DRV8316C compared to discrete solution, the benefits of smaller size and high integration outweigh downsides in sub 250 g UAV applications. As UAVs generate large amount of airflow during operation, it will help ease heat dissipation issues.

2.3.3 Auxiliary converter

The main power consumer on the auxiliary low voltage rail is the MCU. The recommended power supply current rating from the ESP32-S3 datasheet is 500 mA, which rules out the use of DRV8316C integrated auxiliary converter due to 200 mA current limit.

TPS54202 was chosen as external auxiliary converter, as it is capable of 2 A continuous current output, can handle whole voltage range and has synchronous rectification, which reduces board size and improves efficiency.

2.3.4 PCB temperature sensor

To protect printed circuit board (PCB) and inverter from overheating, a temperature sensor is placed on PCB to provide temperature feedback and prevent exceeding the component temperature limits. For cost-effective measurement of PCB temperature,

Negative Temperature Coefficient (NTC) thermistors and Linear Active Thermistor ICs are considered.

While NTC thermistors have smaller package and typically offer lower cost, they require signal conditioning circuit and complex calculation to converter the resistance into temperature. Active Thermistor ICs on the other hand have signal conditioning inside IC and output linear voltage signal relative to temperature sensed. Author chose **MCP9700T** temperature sensor for the ESC due to ease of integration and linear temperature relationship.

2.3.5 Status LED

As was discussed in the solution proposal, the best user experience was offered by a RGB LED. For controlling one RGB LED, both analog and digital LED solution are acceptable.

Analog LEDs require each colour of LED to be controlled separately by a PWM signal. This approach requires three GPIO pins to be separately routed to the LED with a current limiting resistor for each LED. On other hand, while having a higher price point, a RGB LED with a digital controller inside the LED requires only one GPIO pin and doesn't require current limiting resistors. This offers lower PCB area and simplified PCB routing.

Due to points above, good component availability and wide software support, a **WS2812B** LED was chosen for the ESC.

2.4 ESC mathematical modelling

2.4.1 ESC Simulink simulation

To make sure proposed solution has no significant fundamental issues and to verify that FOC offers lower input power consumption over 6-step commutation, a Simulink model was created and simulated in MATLAB software.

Existing blocks from Simscape toolbox were used to create a simplified model of the two ESCs (see full model in Appendix 2). MCU was replaced by respective 6-step and FOC motor control blocks, three phase inverters used MOSFETs, and PMSM block parameters were adjusted to fit parameters from Table 2.2. Input voltage was set to 24 V, target

speed was set to 3500 rpm and a 5 mNm load was applied to rotor to test operation under load.

Steady state simulation results can be seen on Figure 2.3. The first 8 seconds of the simulation are not shown, as it included dynamic processes of electrical machine startup and acceleration to setpoint. As both ESC models successfully started electrical machines and reached target speeds, proposed solution can be considered valid and proceeded with detailed design process.

A clear difference in input power was observed between 6-step and FOC ESC. At steady state, FOC ESC had ~35 % lower input power compared to 6-step ESC. FOC ESC input and motor power had significantly lower ripple and overall offered smoother performance.

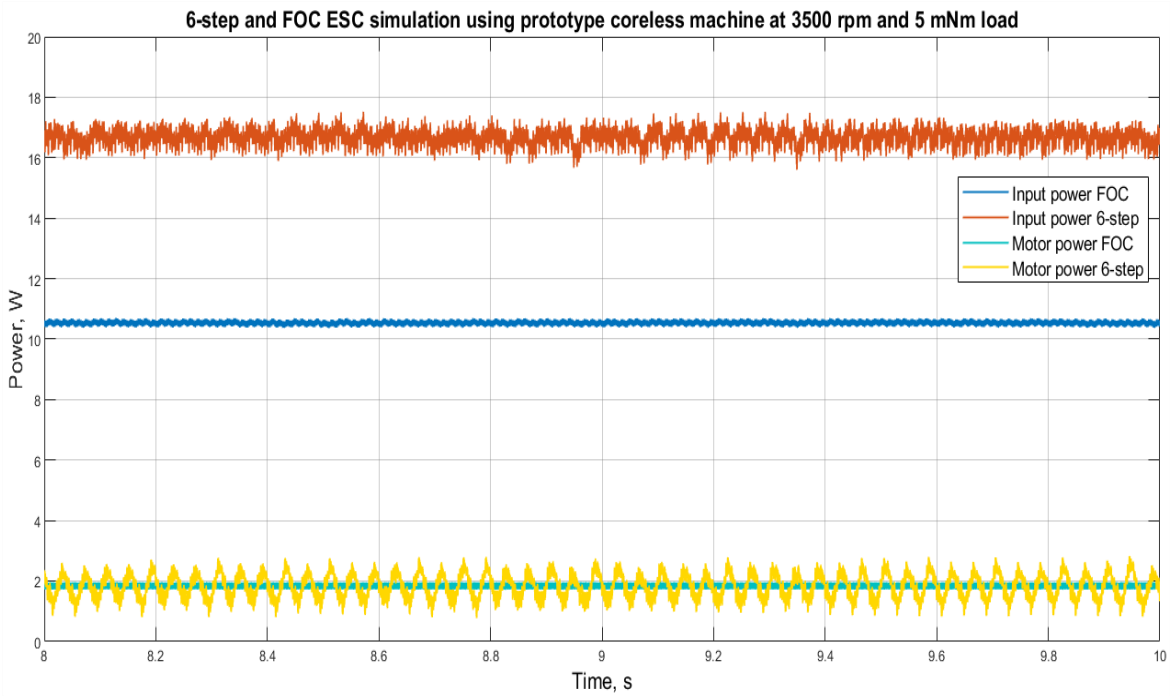

Figure 2.3 6-step and FOC ESC simulation in MATLAB Simulink

2.4.2 DRV8316C thermal calculations

To verify that PCB can handle DRV8316C power dissipation at maximum phase current, thermal calculations need to be done and verified DRV8316C maximum junction temperature of 150 ºC won't be exceeded. First FET conduction and FET switching losses are calculated based on formulas provided in the DRV8316C datasheet [30]. Based on the losses and thermal resistances of the IC, the final junction temperature can be calculated.

As heat generating components are mounted on the PCB and PCB consists of alternating layers of dielectric and copper, the resulting thermal analysis is significantly complicated, and simple analytic solution is not possible. Additionally, the thermal resistance values provided by the datasheet depend largely on the PCB design. Due to points highlighted before and to not exceed the scope of the thesis, a sophisticated online PCB temperature calculator [31] was used to estimate thermal performance with natural convection and at forced convection speeds of 1 - 3 m/s.

FET conduction losses were calculated using Equation 2.1. The conduction losses were calculated at 5 A phase current, which is the worst-case scenario that still meets the specification.

$$P_{con} = 3 \cdot (I_{rms})^2 \cdot R_{ds,on} = 3 \cdot (I_{rms})^2 \cdot R_{ds,on} = 3 \cdot 5^2 \text{A} \cdot 0{,}095\ \Omega = 7{,}13\ \text{W} \qquad (2.1)$$

where P_{con}- FET conductive losses, W,
I_{rms}- ESC rms phase current, A,
$R_{ds,on}$- Total FET on resistance, Ω.

FET switching loss formula was adjusted to include FET slew rate and input voltage instead of rise and fall time, resulting in Equation 2.2. The switching losses were calculated using switching frequency of 25 kHz, input voltage of 25,6 V, and FET slew rate of 200 $\frac{\text{V}}{\mu\text{s}}$.

$$P_{sw} = 3 \cdot I_{rms} \cdot V_{peak} \cdot \frac{V_{peak}}{slew_{FET}} \cdot f_{PWM} = 3 \cdot I_{rms} \cdot \frac{{V_{peak}}^2}{slew_{FET}} \cdot f_{PWM} =$$

$$= 3 \cdot 5\ \text{A} \cdot \frac{25{,}6\ \text{V}^2}{200 \frac{\text{V}}{\mu\text{s}}} \cdot 25\ \text{kHz} = 1{,}23\ \text{W} \qquad (2.2)$$

where P_{sw}- FET switching losses, W,
I_{rms}- ESC rms phase current, A,
V_{peak}- Maximum input voltage, V,
$slew_{FET}$- FET slew rate, $\frac{\text{V}}{\mu\text{s}}$,
f_{PWM}- FET switching frequency, Hz.

$$P_{total} = P_{FET} + P_{sw} = 7{,}125\ \text{W} + 1{,}23\ \text{W} = 8{,}36\ \text{W} \qquad (2.3)$$

where P_{total}- Total IC losses, W.

The total losses calculated from equation 2.3 are comparably high, so likely additional heatsink on top of IC would be needed to not exceed maximum junction temperature. If not for the additional airflow from the propellers, this high of a power dissipation would be challenging to remove from PCB without use of forced convection.

PCB heat dissipation and IC Junction temperatures are calculated using a sophisticated PCB temperature calculator [31]. Below list can be found with all parameters used to in the calculator:

- Driver IC maximum acceptable junction temperature of 135 ºC, ambient temperature of 20 ºC,
- Square PCB with dimension 40x40 mm, four 35 µm copper layers with 60 % coverage, PCB Emissivity 0,75
- Driver IC thermal pad dimension 5,5x3,8 mm, junction to board thermal resistance 7,3 ºC/W, junction to top case thermal resistance 15,2 ºC/W, IC package emissivity 0,9
- Thermal vias enabled at default settings

From Figure 2.4 can be seen, that without heatsink maximum phase current was ~4,1 A. So, to meet the 5 A phase current specification, a heatsink must be used to increase heat dissipation from top of the IC and bring junction temperature to acceptable levels.

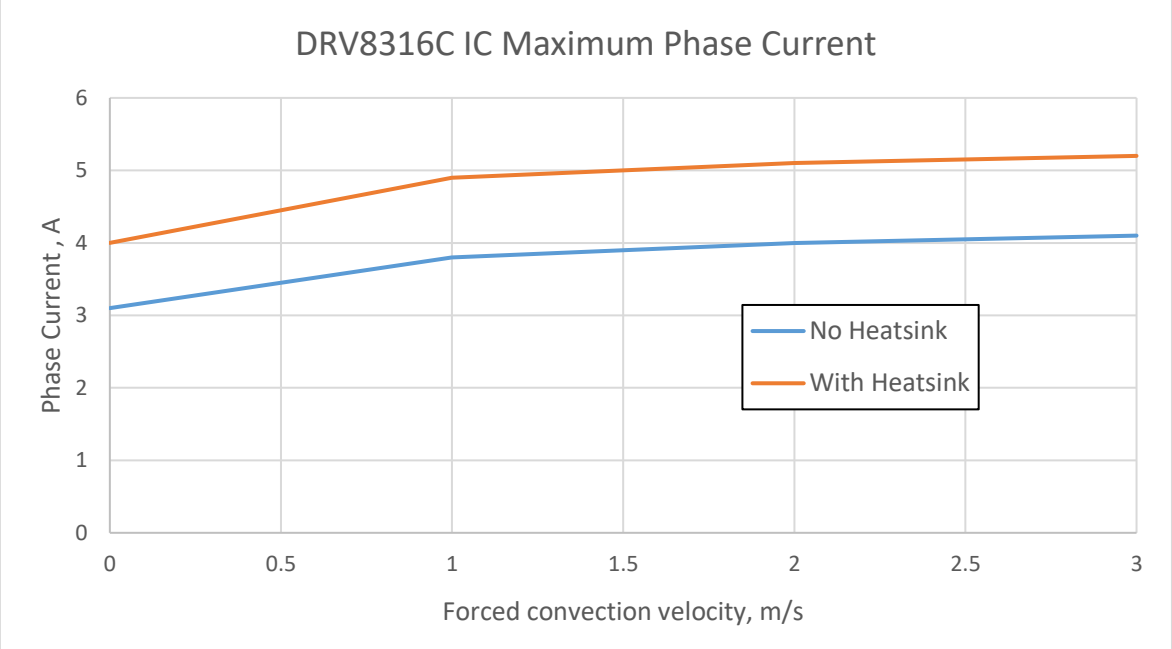

Figure 2.4 DRV8316C Motor Driver IC maximum phase currents without and with HSB02-101007 heatsink between forced convection velocities of 0 and 3 m/s

HSB02-101007 heatsink was chosen to be placed on top of IC, as its size of 10 mm by 10 mm is close to the size of IC and includes thermal resistance data for natural convection, forced convection at 1 and 2 m/s [32]. 2 m/s thermal resistance is used also for 3 m/s calculation.

Use of small heatsink significantly improved overall thermal performance of the PCB (see Figure 2.4). The 5 A phase current specification wasn't met with natural convection and at 1 m/s forced convection but at 2 m/s or above air velocities, 5 A phase current operation was achieved. Buffer of 15 ºC was included between DRV8316C IC absolute maximum junction temperature and calculations in Figure 2.4 to have margin for safe operation. Based on calculations and figures shown before, author is confident that prototype FOC ESC won't overheat during operation at high phase currents.

2.5 ESC PCB design

After thermal calculations were completed, author proceeded with the PCB design process. The PCB design can be divided into three main parts: Schematic drawing, PCB routing and manufacturing. First two parts are done by the author and last part by a dedicated fabrication house.

Only major choices and decisions that were not explained by previous sections will be handled by this section. It is important to highlight that due to proof-of-concept design, safe approach to PCB design was taken. The design layout shown in Figure 2.5 is unoptimized and can easily be improved in future reversions. All design files relevant to prototype FOC are accessible from Appendix 3.

2.5.1 PCB schematic

Wherever possible, author followed the design recommendations and relevant application examples, especially for MCU and Motor driver IC. As this design is a prototype, minor adjustments were made to simplify testing process.

Connectors and screw terminals are used instead of just pads for connections to avoid need of soldering and unsoldering wires directly to PCB (see Appendix 1). To meet sensor specification, a separate 6 pin connector was added and connected to the MCU. USB-C connector is used to provide power and programming interface. A 4-pin connector was added as separate control signal connection. All external connections

have Electrostatic Discharge protection to protect the MCU. Place for additional bulk capacitor was added at position C16.

2.5.2 PCB layout and routing

A 4-layer PCB configuration was chosen due to improved heat transfer capability and large number of connections and surface mount devices used in the design.

A set of thermal vias were placed under DRV8316C IC to bring heat away from the IC and reduce PCB thermal resistance. The copper planes were designed to not have large plane cuts to not trap heat and help with heat transfer. PCB temperature sensor was placed on opposing side close to thermal vias. Decoupling capacitors were placed as close to the ICs as possible. Designators and additional text were placed to improve user friendliness. The manufactured PCB can be seen on Figure 2.5.

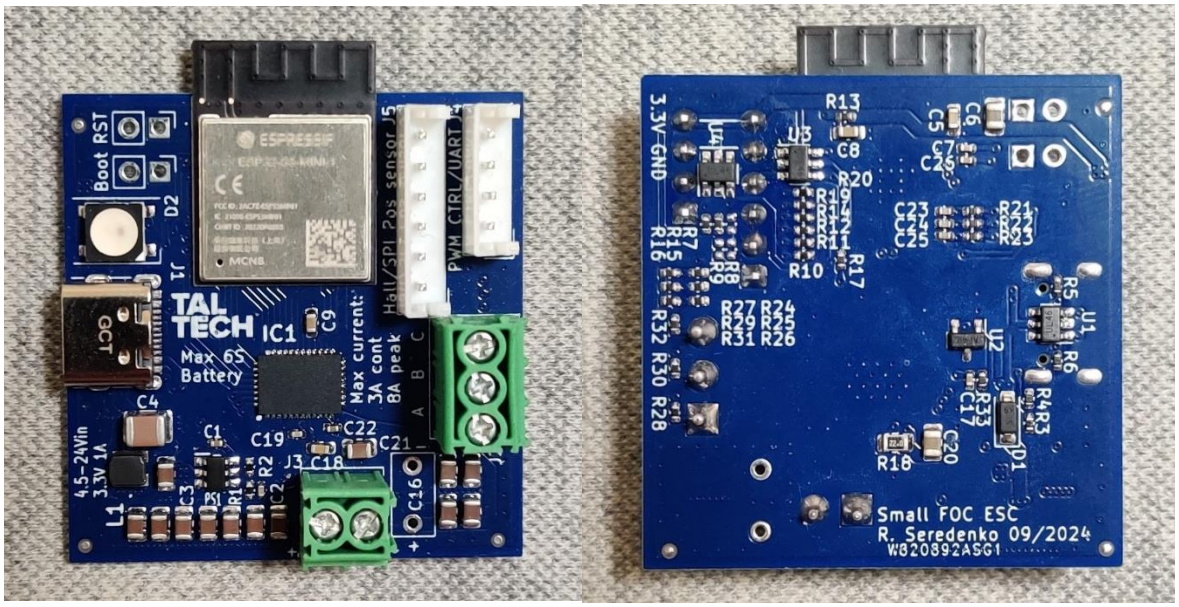

Figure 2.5 Manufactured prototype FOC ESC PCB

2.6 ESC Firmware

While it is important to get the hardware design correct, the firmware on the MCU is what controls the hardware and provides the ESC functionality. To simplify firmware and avoid writing FOC library from the scratch, an open-source SimpleFOC library [25] is used as core for the firmware. SimpleFOC has existing support for many MCU families, excellent documentation with many examples, drivers for common motor driver ICs and

active community. The ESC firmware is entirely open source and available in Appendix 3.

One of SimpleFOC benefits is in its modularity and high level of abstraction. While out of the box SimpleFOC library has support for only sensored FOC, by use of a Flux Observer from another open-source project MESC [33], sensorless FOC was made possible.

ESP32-S3 ADC driver was changed to improve sensorless FOC performance and SimpleFOC was also adapted for dual core use, as ESP32-S3 has 2 cores and offered smoother operation. In addition to SimpleFOC core library, the DRV8316C drivers were used from Simple-FOC-Drivers library [34]. Code from library offered good starting point but had to be modified to include error checking and fault handling.

For controlling the digital LED, Adafruit_Neopixel library [35] was used. No modifications were made to this library, as functionality offered by the library was satisfactory to control the LED and no other special requirement was required by the specification.

3 DESIGN VERIFICATION AND EXPERIMENTS

This chapter is divided into three parts: design verification, experimental results, and result analysis and future improvement sections. The design verification section lists verification criteria, verification setups and verification result for each criterion. The experimental result section describes planned experiments, equipment used in experiments and presents results and figures from the gathered experimental data. In the last section the results from the second section are analyzed, conclusions are drawn and future improvements to ESC proposed.

3.1 Prototype ESC design verification

Majority of the experiments were done in the prototyping laboratory in the Department of Electrical Power Engineering and Mechatronics. There safe electrical machine experiment environment was present, with a metal cage to protect the user in case of accidents and wide variety of tools and instruments necessary for test setups.

3.1.1 Design verification setup

Design verification is important part of product design and results from design verification are used to evaluate and find issues with the design. As thorough design verification can be a lengthy process and is not the main topic of this thesis, only key components listed below are verified as a compromise. Specification is used to select components for verification and reasonable pass conditions are selected based on component capability and use case. Below is a test protocol along a condition that must be satisfied at each step:

Auxiliary 3,3 V converter:

Pass condition: Converter output 3,3 V ± 5 % across the whole input voltage range 6-25,6 V.

DC-bus voltage:

Pass condition: DC-bus voltage measurement deviation below ± 5 % across whole voltage range.

Temperature sensor:

Pass condition: Temperature sensor measurement deviation below ± 3 ^{o}C

Status LED:

Pass condition: Status LED displays all colors correctly.

Motor driver IC:

Pass conditions:

ESC is capable to generate sinusoidal and SVM output waveform.

ESC reported rotor speed deviation below ± 3 %.

For 3,3 V converter and DC bus voltage measurement, OWON HDS272S in digital multimeter (DMM) mode is used to measure reference voltage. Temperature sensor measurement is verified using a non-contact method with a FLIR TG275 thermal camera. ESC output waveform is verified using oscilloscope mode on OWON HDS272S. Rotor speed is measured using an optical tachometer. Status LED colour accuracy is verified visually.

3.1.2 Design verification results

Design verification is done step by step in accordance with the item 3.1.1.

Auxiliary 3,3 V converter:

Pass condition: Auxiliary converter outputs 3,3 V ± 5 % across the whole input voltage range of 6 - 25,6 V. Reference voltage was measured using OWON HDS272S DMM.

3,3 V rail converter stayed within specification across whole input voltage range. Individual measurement result can be seen in the Table 3.1.

Table 3.1 Auxiliary 3,3 V converter measurement results

Input voltage	3,3 V rail voltage	Measurement error	Result
6 V	3,280 V	<1 %	Pass
12 V	3,281 V	<1 %	Pass
15 V	3,281 V	<1 %	Pass
20 V	3,281 V	<1 %	Pass
25,6 V	3,280 V	<1 %	Pass

DC-bus voltage:

Pass condition: DC bus voltage measurement deviation below ± 5 % across whole voltage range. Reference voltage was measured using OWON HDS272S DMM.

From Table 3.2 can be seen, that although DC bus voltage reported by ESC had fluctuations, it significantly exceeded ± 5 % specification.

Table 3.2 DC bus voltage measurement results

DMM measured DC bus voltage	DC bus voltage reported by ESC	Measurement error	Result
6,01 V	5,98 V	<1 %	Pass
12,02 V	12,08 V	<1 %	Pass
16,01 V	15,94 V	<1 %	Pass
20,02 V	19,95 V	<1 %	Pass
24,00 V	23,99 V	<1 %	Pass

Temperature sensor:

Pass condition: Temperature sensor measurement deviation below ± 3 ºC. Reference temperature was measured using FLIR TG275 temperature sensor.

Two realistic temperature measurement points were chosen as achieving arbitrary temperature values is non-trivial and requires expensive equipment. In addition, low temperature measurement accuracy is not critical in current ESC, as DRV8316C IC has additional built in over-temperature protection.

Two temperature points chosen were 25 ºC and ~50 ºC. In both cases measurement was taken after 10 minutes so prototype ESC PCB could reach temperature equilibrium. As can be seen from Table 3.3, in both cases ESC met the specification. Heat distribution and temperatures from thermal camera can be seen on Figure 3.1.

Table 3.3 Temperature sensor measurement results

Thermal camera temperature measurement	PCB temperature reported by ESC	Measurement error	Result
25,0 ºC	23 ºC	2 ºC	Pass
47,4 ºC	49 ºC	1,6 ºC	Pass

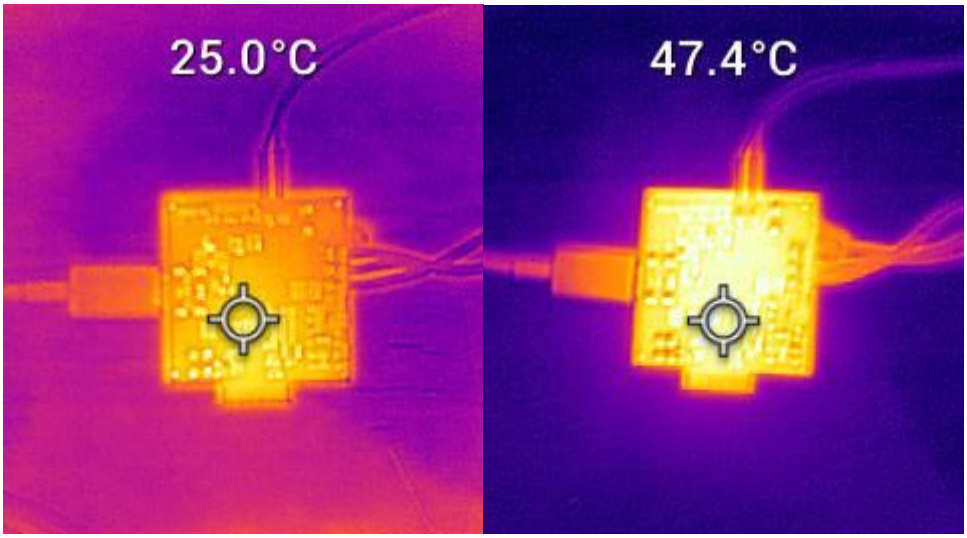

Figure 3.1 Prototype ESC thermal images with FLIR TG275

Status LED:

Pass condition: Status LED displays all red, green, blue colors correctly.

LED used on author's ESC has an integrated driver IC inside the LED package, so instead of driving three individual LEDs directly, a bitstream in correct format needs to be generated and sent to LED. As mentioned in the item 2.3.5, an existing open-source Adafruit library was used to generate bitstream and control LED.

LED operation was verified visually by enabling individually red, green and blue LED channels. As can be seen from Figure 3.2, all three LEDs showed correct colours.

Result: **Pass**.

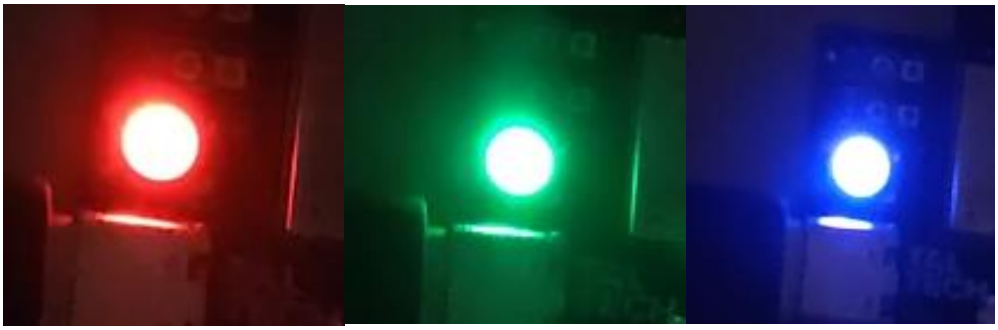

Figure 3.2 Red, green and blue LED colour operation verification

Motor driver IC:

Pass condition: ESC is capable to generate sinusoidal and SVM output waveform.

As was previously discussed, a sinusoidal waveform is optimal for a coreless electrical machine. Due to this, it is important to verify that ESC output is indeed sinusoidal. PWM switching is done at high frequency, so to bring out the sine wave, waveform capture requires passing through a filter to show sinusoidal pattern. SVM waveform generation is also verified so ESC can leverage improved DC-bus voltage utilization. As can be seen from Figure 3.3, both filtered outputs successfully produced desired waveform.

Result: **Pass**.

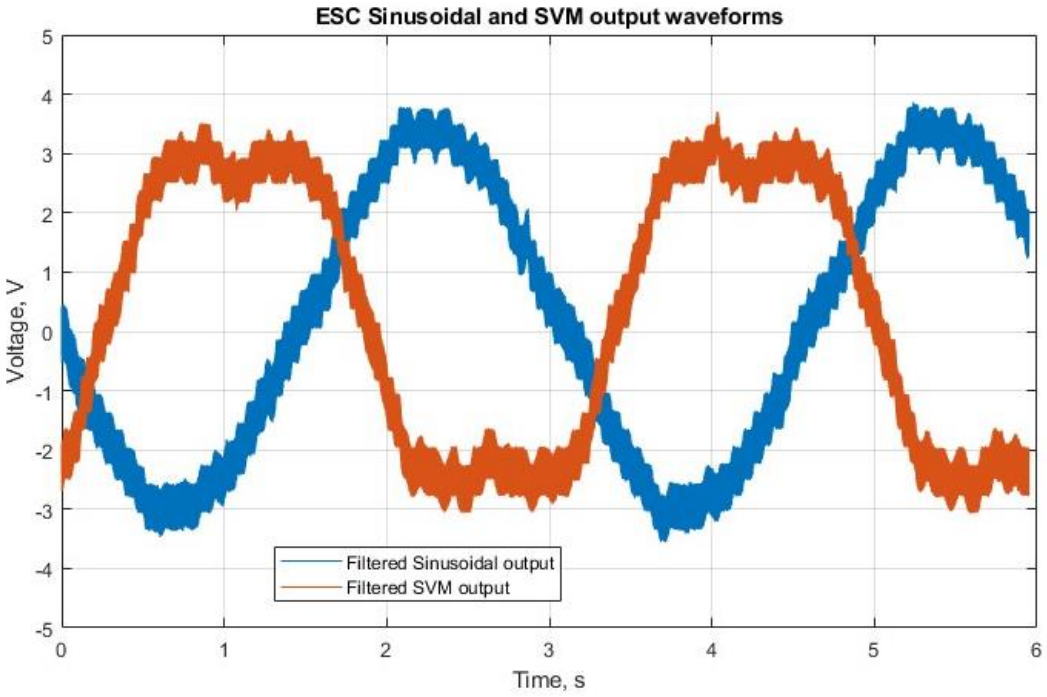

Figure 3.3 ESC sinusoidal and SVM output waveforms

Pass condition: ESC reported rotor speed deviation below ± 3 %.

From Table 3.4 can be seen, that rotational speed was accurate across whole range and measurement error significantly exceeded ± 3 % specification.

Result: **Pass**.

Table 3.4 Angular velocity measurement results

Tachometer measured speed, rpm	Speed reported by ESC, rpm	Measurement error	Result
765	765,2	<0,1 %	Pass
1957	1957,6	<0,1 %	Pass
2980	2980,2	<0,1 %	Pass
4965	4965,9	<0,1 %	Pass
6718	6720,2	<0,1 %	Pass

3.2 Experimental results

3.2.1 ESC input power and efficiency measurement setup

While creation of test protocol for the design verification setup is relatively simple, accurate efficiency measurement of the three-phase electrical machine is nontrivial and requires significantly more careful approach.

Efficiency is relationship between machine input electrical power and output mechanical power (see Equation 3.2). One way of comparing different ESCs is by measuring the absolute efficiency of the ESC and coreless machine combinations and comparing absolute values. While this approach provides absolute efficiency value, it requires setup and equipment capable of measuring the electrical machine's rotor torque and speed (see Equation 3.1). Due to the small size and lack of iron core, torque produced by the prototype coreless machine is low and the torque measurement equipment will have large measurement error, which increases result uncertainty.

$$P_{mech} = \tau \cdot \omega \tag{3.1}$$

where τ – rotor torque, Nm,

ω – rotor angular velocity, rad/s.

To solve problems mentioned above, author proposes the use of comparative efficiency measurement instead of absolute efficiency measurement. By applying a known load like a propeller to the machine shaft at set speed, it will result in a same load applied to the machine regardless of the commutation algorithm. By measuring the input power consumed by the ESC, it is possible to directly compare results between different devices. While this approach won't provide accurate absolute efficiency value, it will have significantly lower measurement uncertainty by only requiring accurate rotor speed measurement. The second approach in addition to lower uncertainty is also closer to the real-world application, where measured efficiency improvement can directly be translated into longer flight time of UAVs.

Nevertheless, efficiency and power consumption map are created by using estimated torque values from simulated propeller performance data [36] and extrapolating for missing datapoints. As extrapolated data in both cases is based on rotor speed, it won't create increased measurement uncertainty and ESC maps can be used for comparison between each other, but as explained earlier, absolute efficiency value will not be accurate.

As ESCs are powered by DC source, input power measurement is simple using two DMMs. Voltage measurement from first DMM is multiplied by current measurement from second DMM and results in the input power consumption. As input is a DC source, no additional considerations are needed about the source power factor, only requirement is a true-RMS capable DMMs.

6-step ESC with comparable parameters to the prototype FOC ESC was used for experiments. As prototype coreless machine has relatively high stator resistance and inductance, multiple settings were tuned for more stable performance. Demagnetization compensation was set to maximum, motor commutation timing adjusted to 25 degrees and PWM frequency set to 25 kHz, equal to the prototype FOC ESC. Ramp-up power was set to 150% to improve startup reliability.

An optical rotational probe from Tyto Robotics Series 1585 thrust stand is used for rotor speed measurement and two OWON HDS272S in DMM mode are used for input current and voltage measurements.

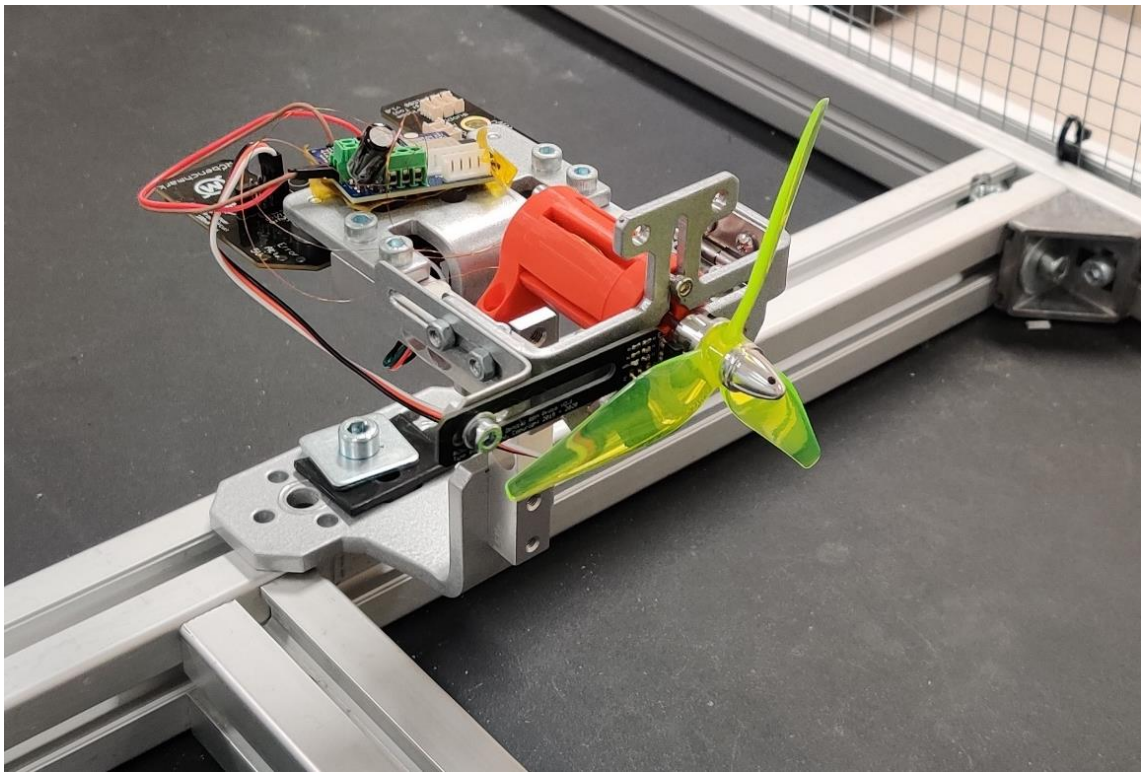

Figure 3.4 Tyto Robotics 1585 thrust stand with prototype FOC ESC and prototype coreless machine mounted with 100 mm propeller

Different load scenarios are applied to get data from working at different operation points. Measurements are made with same load attached to both ESCs. ESCs are tested in three load scenarios: light load, medium load and large load.

Light load scenario uses a relatively small triple-blade 100 mm diameter and pitch propeller, so machine will still operate at high speeds. A 152 mm diameter and 107 mm pitch dual-blade propeller with is used as medium load, where machine will operate at medium speeds. For large load scenario, a 254 mm diameter and 114 mm pitch dual-blade propeller is used to simulate low speed and high torque operation. Comparison between propeller sizes can be seen on Figure 3.5.

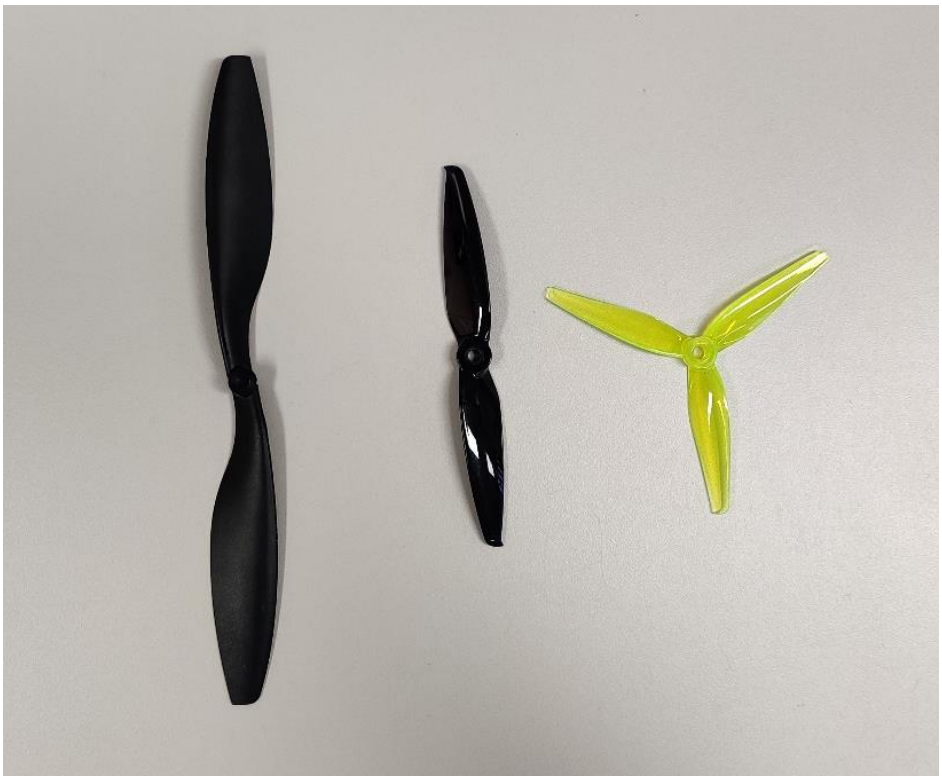

Figure 3.5 254 mm, 152 mm and 100 mm diameter propellers used in experiments

3.2.2 ESC input power and efficiency measurement results

ESC Input Power measurements relative to the propeller rotational speed are presented using three separate figures (see Figure 3.6 - Figure 3.8). Each figure shows input power measurements of 6-step and prototype FOC ESC. The ESC input power increases non-linearly, following a general upward curve, which aligns with the expected cubic relationship between rotational speed and power for propellers. The start and end points of the data indicate the stable minimum and maximum operating speeds of the respective ESCs.

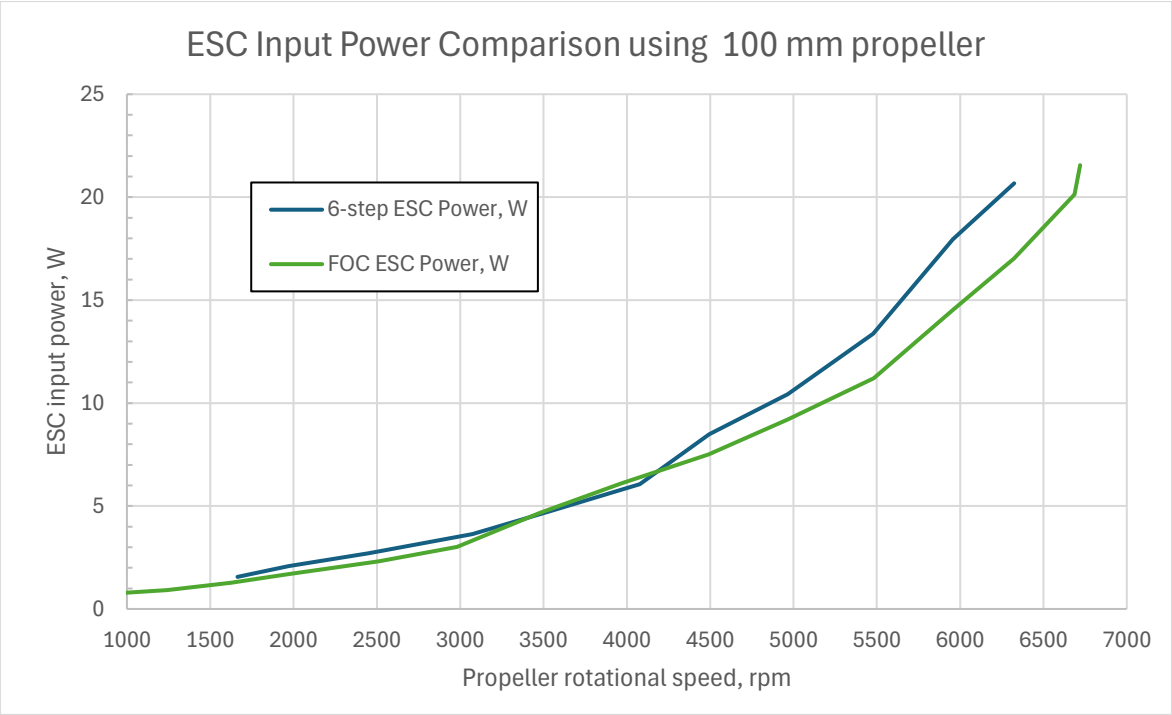

Figure 3.6 ESC Input Power comparison between prototype FOC ESC and commercial 6-step ESC with a triple-blade 100 mm propeller attached to prototype coreless machine

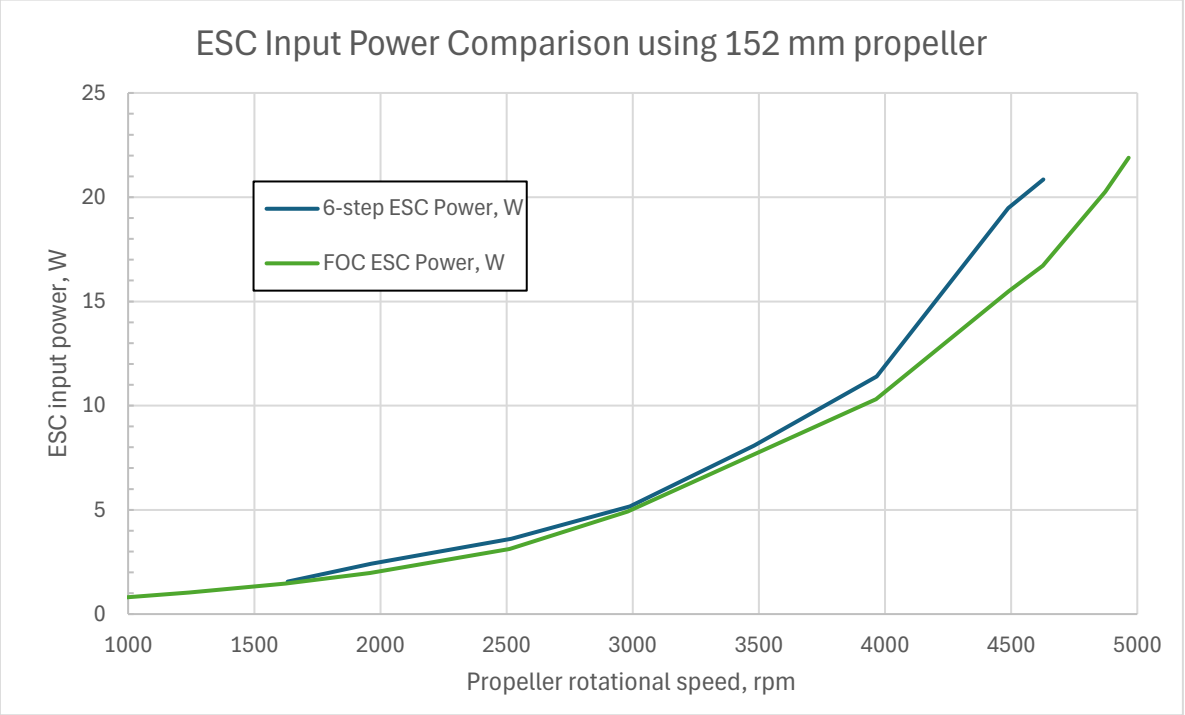

Figure 3.7 ESC Input Power comparison between prototype FOC ESC and commercial 6-step ESC with a dual-blade 152 mm propeller attached to prototype coreless machine

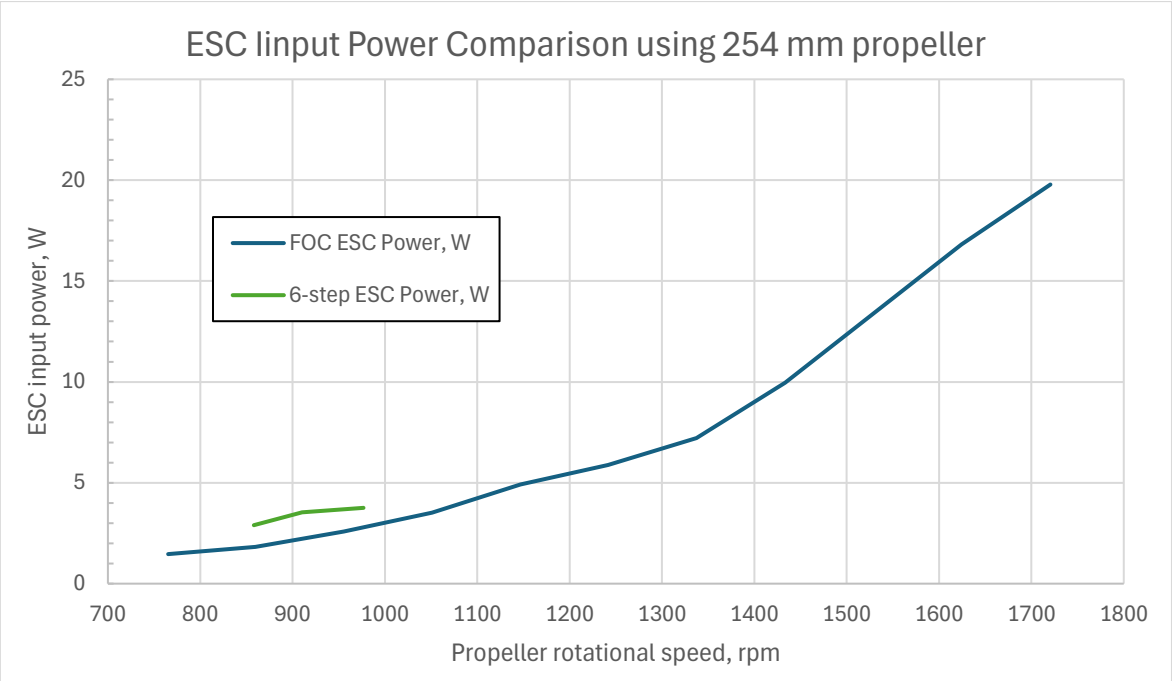

Figure 3.8 ESC Input Power comparison between prototype FOC ESC and commercial 6-step ESC with a dual-blade 254 mm propeller attached to prototype coreless machine. The short 6-step ESC line was result of poor ESC performance.

To enhance the visualization of ESC results, rotor torque was derived from simulated propeller data [36] for each propeller. Input power and estimated coreless machine efficiency (See Equation 3.2) maps were created for both ESCs. For easier comparison between 6-step and prototype FOC ESC figures, torque, speed and input power or machine efficiency axis spans were kept equal.

$$\eta_{machine} = \frac{P_{mech}}{P_{input}} \cdot 100\% \tag{3.2}$$

where $\eta_{machine}$ – Electrical machine efficiency, %,

P_{input} – Input power, W.

The data presented in the following figures should be interpreted with caution, as rotor torque values were indirectly estimated, and parasitic losses were not accounted for. As a result, the absolute efficiency values will not be accurate. However, the results remain valid for comparative analysis, as they are derived from low-uncertainty data. The artifacts observed in the prototype FOC ESC maps are a consequence of the rotor torque approximation, which is limited by the availability of propeller data at 1000 rpm intervals.

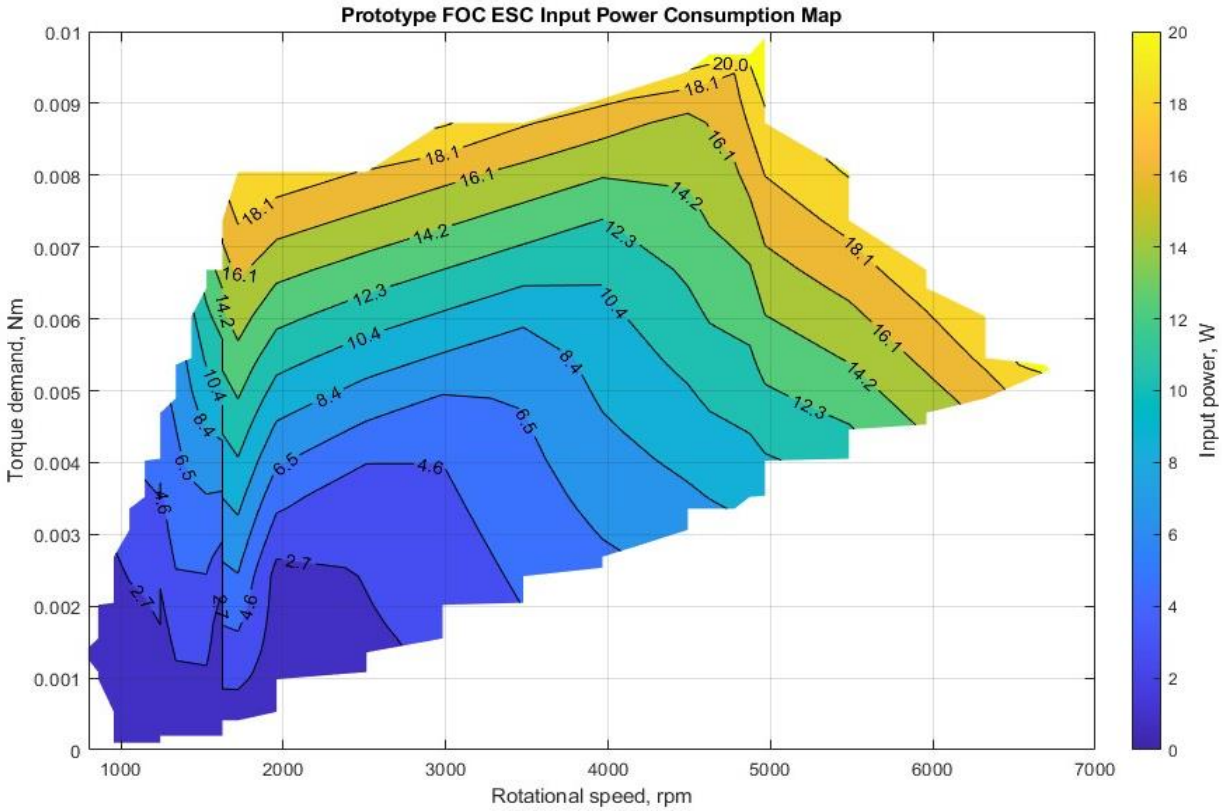

Figure 3.9 Prototype FOC ESC Input Power Consumption Map

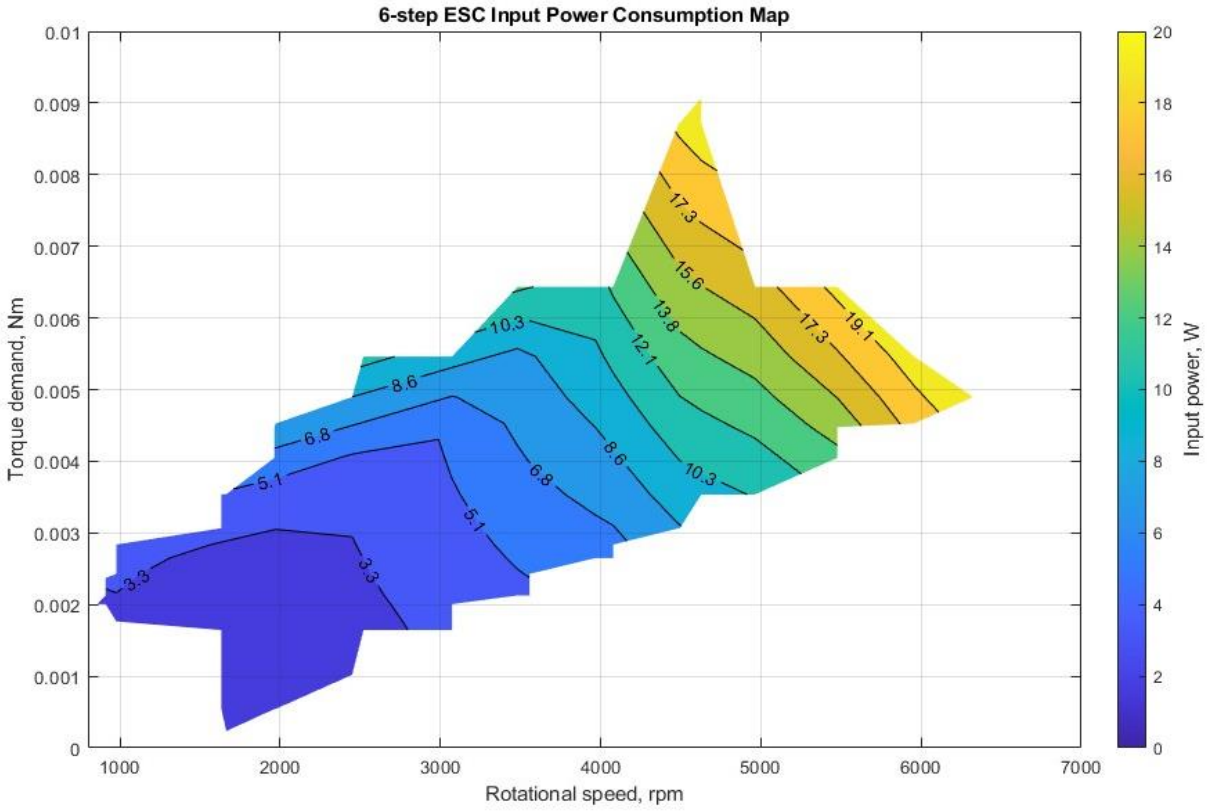

Figure 3.10 Commercial 6-step ESC Input Power Consumption Map

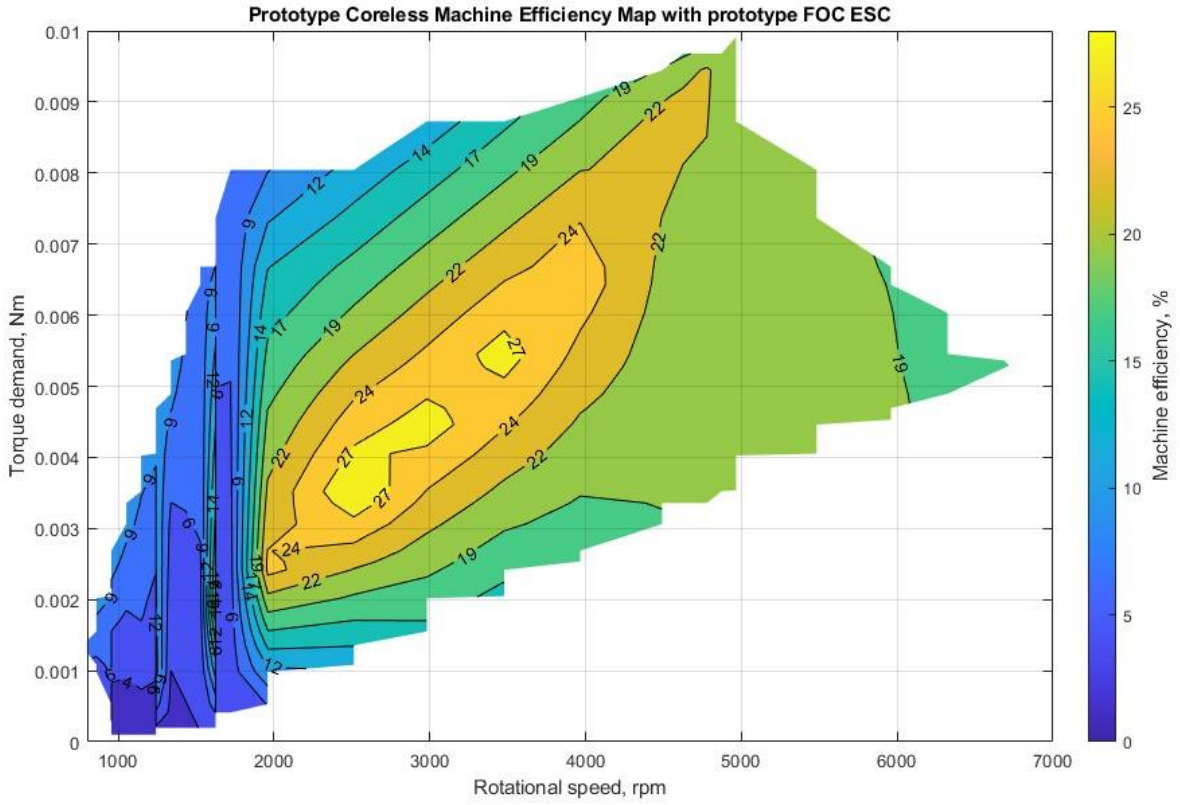

Figure 3.11 Estimated prototype Coreless Machine Efficiency Map using prototype FOC ESC

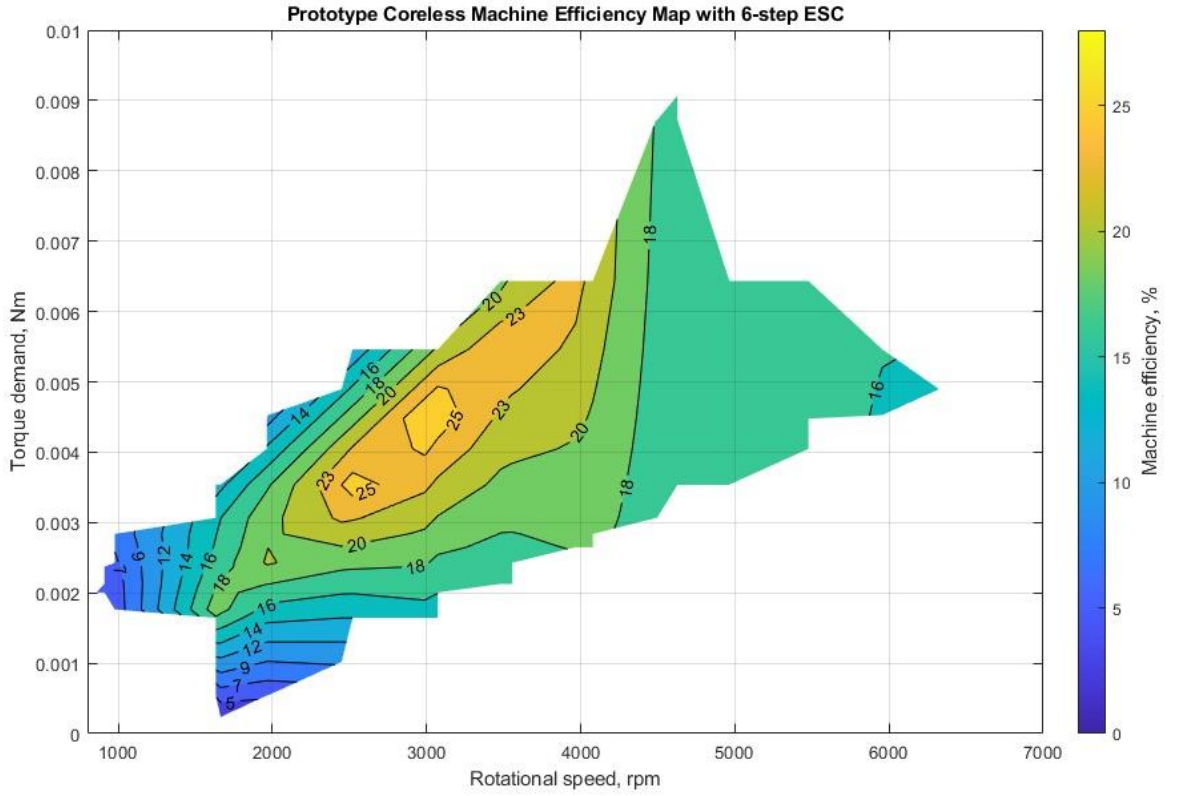

Figure 3.12 Estimated prototype coreless Machine Efficiency Map using commercial 6-step ESC

3.3 Result analysis

The trends observed in Figure 3.6 and Figure 3.7 indicate that at low propeller speeds, the input power of the prototype FOC ESC is slightly lower compared to the commercial 6-step ESC. At medium propeller speeds, both ESCs exhibit nearly identical input power consumption. However, at 4000 rpm with the 100 mm propeller, the 6-step ESC demonstrated marginally lower input power than the prototype FOC ESC. This trend reverses significantly at high propeller speeds, where the prototype FOC ESC achieves notably lower input power consumption.

To illustrate the potential benefits, when a commercial 6-step ESC was replaced with the prototype FOC ESC in a UAV using prototype coreless machine with a 152 mm propeller and operated at 4500 rpm, FOC ESC could extend the flight time by up to **20 %**, if power consumption of other UAV components is ignored. Additionally, as the machine phase currents are lower at equivalent propeller speeds, further flight time improvements could be realized by utilizing smaller, lower-rated inverter components. This would reduce the ESC size and weight, leading to improved UAV performance.

The observed input power consumption trends (Figure 3.6 and Figure 3.7) may stem from the inherent characteristics of sensorless 6-step commutation. As shown in Figure 1.4, 6-step commutation relies on back-EMF zero-crossing detection with a programmed offset angle. For the commercial 6-step ESC used in the experiments, an offset angle of 25° was programmed. While this angle provided optimal performance at medium speeds, the fixed commutation timing proved suboptimal at low and high speeds, leading to decreased coreless machine efficiency and increased power consumption. The inability of the 6-step ESC to dynamically adjust commutation timing during operation likely contributed to these inefficiencies.

Figure 3.8 further highlights the limitations of the 6-step ESC in low-speed torque control and dynamic performance. When driving the 254 mm propeller, which has greater size, weight, and inertia, the commercial 6-step ESC failed to control the prototype coreless machine effectively. Specifically, the 6-step ESC could only sustain operation between 860 rpm and 980 rpm, whereas the prototype FOC ESC successfully operated within a wider speed range of **765 rpm to 1720 rpm**. Similar results were observed with the 100 mm and 152 mm propellers, where the prototype FOC ESC demonstrated superior low-speed performance, spinning the propellers below 1000 rpm and achieving several hundred rpm higher speeds compared to the 6-step ESC.

Figure 3.10 through Figure 3.12 further visualize the deficiencies of the 6-step ESC in low-speed, high-torque performance. The 6-step ESC achieved 8 mNm torque only at

speeds around 4500 rpm. In contrast, the prototype FOC ESC consistently generated 8 mNm torque across a significantly broader range, from **1700 rpm to 5500 rpm**. This extended operating range reflects the superior performance of the prototype FOC ESC. Furthermore, Figure 3.11 demonstrates increased peak and overall efficiency of the coreless machine when operated by the prototype FOC ESC.

In summary, the prototype FOC ESC not only outperforms the commercial 6-step ESC in terms of power consumption at high speeds but also provides superior torque control, dynamic response, and operational range across varying propeller loads and speeds. These findings confirmed statements from literature review and underscore the benefits of implementing Field-Oriented Control for coreless machines, particularly in applications requiring high efficiency and broad speed-torque performance.

3.4 Future improvements to prototype FOC ESC and experiments

3.4.1 Microcontroller choice

The selection of the **dual-core ESP32-S3 MCU**, in retrospect, was not ideal for this application. While it demonstrated no major issues controlling electrical machines at 100000 electrical rpm and has processing capacity for higher speeds, its primary limitation lies in its relatively slow built-in ADC. The prototype FOC ESC uses a single ADC for all three-phase current measurements, effectively dividing the ADC's sampling rate by three. Additionally, the same ADC is used for DC-bus and temperature measurements, which can cause machine stuttering if these measurements are polled too frequently.

Even with an interleaved configuration using the ESP32-S3's two ADCs, simultaneous sampling of all three current channels is not achievable, resulting in measurement delays. These delays, coupled with the reduced overall sampling rate, impose a limitation on the maximum rotational speed of the ESC due to the constraints of low-side current sensing.

To address these limitations, two potential approaches are proposed:

1. **Upgrading the MCU**: Replacing the ESP32-S3 with an MCU featuring more and faster ADCs, such as those from the STM32F4 or STM32G4 series, could solve the sampling rate issues while retaining the low-side current sensing configuration. These MCUs, although single-core, are equipped with hardware trigonometric accelerators, providing sufficient computational power for sensorless FOC. An additional advantage of using STM32 MCUs is the ability to transition to alternative open-source libraries, such as MESC [33], which offer greater flexibility in software selection.

2. **Adopting Inline Current Sensing**: Transitioning from low-side current sensing to inline phase current sensing will eliminate the dependence on low-side MOSFET conduction timing for current measurement. This approach ensures continuous phase current measurement and reduces effect of the ADC sampling speed. Furthermore, it allows for significantly higher PWM switching frequencies, as ADC sample times no longer constrain the minimum MOSFET conduction time. However, this solution comes with trade-offs, including increased PCB size requirements, additional current sensing hardware, and higher overall costs.

3.4.2 DRV8316C Motor Driver IC choice

The DRV8316C proved to be a generally effective choice due to its comprehensive protection features and high configurability, which were important in protecting both the ESC and the coreless machine. Additionally, the integrated shunt-less current sensing significantly simplified PCB design and eliminated power losses typically associated with current measurement circuits.

The primary drawback of the DRV8316C lies in its high MOSFET conduction resistance. When continuous phase currents approach 4 A, the heat generated by the IC increases substantially, and without a heatsink or constant forced convection, the overtemperature protection can be triggered.

For applications where the electrical machine is designed to operate at high voltage and low current, the DRV8316C is an excellent fit. However, for systems with rated phase currents of 4 A or higher, the use of discrete MOSFETs and gate drivers is recommended. At these current levels, the DRV8316C losses begin to overshadow the efficiency gains achieved through the FOC algorithm.

While an **inline phase current sensing** approach is not warranted for integrated motor driver ICs, it becomes a logical choice when employing discrete MOSFET and gate driver configurations. In such setups, current sensing must be implemented separately, making inline sensing a viable and attractive option.

3.4.3 Improvements to experiment setup

While the comparative analysis of two different commutation methods provides an effective approach for evaluating and comparing measurement results, future experiments would benefit from incorporating a dedicated high-accuracy torque sensor. Although simulated propeller data provides torque estimations, the measurement uncertainty associated with this method is too high for reliable use, particularly in cases involving large propellers and low-power electrical machines. In these scenarios, the limited number of available measurement points results in inaccurate extrapolation, further increasing the uncertainty.

4 CONCLUSION

This thesis presents the design, prototyping, and verification of a sensorless Field-Oriented Control (FOC) based Electronic Speed Controller (ESC) for coreless electrical machines. The primary objectives included creating an open-source ESC with hardware comparable to commercially available low-cost ESCs, verifying its functionality on a prototype coreless radial flux permanent magnet (RFPM) machine, and evaluating its performance and efficiency relative to a commercially available 6-step ESC.

The work begins with a thorough literature review, analysing BLDC machine control approaches, including trapezoidal (6-step) commutation, sinusoidal commutation, and FOC, alongside a review of existing ESC solutions. This theoretical groundwork justified the choice of FOC for improved machine efficiency and smoother operation, especially in combination with coreless machines. Additionally, limitations of conventional trapezoidal commutation methods were discussed, highlighting its inefficiency for coreless electrical machines.

In the design phase, hardware and firmware solutions were developed alongside ESC mathematical modelling. The design process included specification definition, component selection, MATLAB Simulink ESC simulation, thermal analysis, and prototype printed circuit board (PCB) design. Simulink simulations confirmed the theoretical advantages of FOC, demonstrating potential 35 % lower input power compared to 6-step commutation under steady-state conditions. A prototype FOC ESC was then constructed using DRV8316C integrated circuit (IC) and ESP32-S3 microprocessor (MCU), integrating SimpleFOC open-source firmware and robust hardware components.

The verification phase confirmed that the prototype FOC ESC met its design specifications, demonstrating its ability to generate sinusoidal and space vector modulated waveforms, accurately track rotor speed, and measure input voltage and PCB temperature. Comparative experiments using a prototype coreless RFPM machine and three different propeller sizes revealed that the prototype FOC ESC achieved broader torque-speed operating ranges, superior low-speed performance, and up to 20 % lower input power consumption compared to the commercial 6-step ESC.

Despite these successes, the author highlights areas for improvement, such as replacement of the ESP32-S3 MCU with STM32 series MCU or exploring inline current sensing to address built-in ADC speed limitations. The DRV8316C IC, while great fit for low-current applications, exhibited high losses at phase currents exceeding 4 A, suggesting the need for discrete MOSFET-based designs for higher-current applications.

In conclusion, the prototype ESC successfully demonstrated sensorless FOC operation on a prototype coreless electrical machine, achieving notable efficiency and performance improvements over a commercially available 6-step ESC. This work provides a foundation for the future development of sensorless FOC ESCs, particularly for small sized UAVs and other low-power applications.

KOKKUVÕTE

Antud lõputöö käsitleb rauavabadele elektrimasinatele mõeldud sensorivaba väljavektorjuhtimisel (FOC) põhineva kiiruskontrolleri (ESC) projekteerimist, prototüüpimist ja valideerimist. Töö peamisteks eesmärkideks oli luua avatud lähtekoodiga ESC, mille riistvara on võrreldav turul olevate madala hinna ESC-dega, testida selle toimimist prototüüp rauavabal püsimagnet elektrimasinal ning hinnata selle jõudlust ja efektiivsust turult saadavatelt 6-sammuga ESC-ga.

Töö algab põhjaliku kirjanduse ülevaatega, kus analüüsitakse harjavaba alalisvoolumasinate juhtimisvõtteid nagu trapetsikujulist (6-sammu) kommutatsiooni, siinuselist kommutatsiooni ja FOC-d, ning tuuakse välja olemasolevad ESC lahendused. Teoreetiline taust õigustas FOC-i valikut, kuna see pakub kõrgemat masina efektiivsust ja tagab selle sujuvama töö, eriti rauavabade masinate puhul. Samuti käsitleti tavapärase trapetsikujulise kommutatsiooni piiranguid, tuues esile selle kommutatsiooni probleeme rauavabade elektrimasinate puhul.

Projekteerimisetapis töötati välja riist- ja tarkvaralahendused koos ESC matemaatilise modelleerimisega. Projekteerimisprotsess hõlmas endas spetsifikatsioonide määratlemist, komponentide valikut, MATLAB Simulink'is ESC simulatsiooni, soojusanalüüsi ja prototüübi trükkplaadi (PCB) disaini. Simulink simulatsioonid kinnitasid FOC teoreetilisi eeliseid, näidates, et stabiilses olekus võib FOC sisendvõimsus olla kuni 35 % madalam võrreldes 6-sammu kommutatsiooniga. FOC ESC prototüüp ehitati kasutades DRV8316C mikrokiipi ja ESP32-S3 mikroprotsessorit (MCU), integreerides avatud lähtekoodiga SimpleFOC tarkvara.

Valideerimisetapp kinnitas FOC ESC prototüübi vastavust spetsifikatsioonidele, näidates selle võimekust genereerida siinus- ja ruumivektormoduleeritud lainekujusid, jälgida täpselt rootori kiirust ning mõõta sisendpinget ja PCB temperatuuri. Kasutades võrdlevat katsemeetodit, rauavaba prototüüp RFPM masinat katsetati kolme erineva suuruse propelleritega. Katsed tulemused näitasid, et prototüüp FOC ESC saavutas laiemaid pöördemomendi- ja kiirusevahemikke, suutis töötada madalamatel kiirustel ning tarbis kuni 20 % vähem sisendvõimsust võrreldes turult saadavaga 6-sammulise ESC-ga.

Hoolimata eelmainitud eelistest, autor toob välja täiustamist vajavaid osi. ESP32-S3 MCU võiks asendada STM32 seeria MCU-ga või võtta kasutusele *inline* tüüpi voolumõõtmist, et lahendada olemasoleva MCU sisseehitatud ADC kiiruse piiranguid. Kuigi DRV8316C sobib hästi madala voolu rakendustes, üle 4 A faasivoolude korral

muutuvad kaod võrdlemisi kõrgeteks, mistõttu autor soovitab kõrgemate faasivoolude korral kasutada diskreetsetel MOSFET-l põhinevaid lahendusi.

Kokkuvõttes, autor demonstreeris prototüüp FOC ESC eduka sensorivaba FOC toimimist prototüüp rauavabal elektrimasinal, saavutades märkimisväärseid efektiivsuse ja jõudluse parandusi võrreldes turult kättesaadava 6-sammulise ESC-ga. See töö loob aluse tulevaste andurivaba FOC ESC-de arendamiseks, eriti väikeste UAV-de ja muude madala võimsusega rakendustes.

REFERENCES

[1] C.-L. Xia, Permanent Magnet Brushless DC Motor Drives and Controls, John Wiley & Sons Singapore Pte. Ltd., 2012.

[2] V. Carev, J. Roháč, M. Šipoš and M. Schmirler, "A Multilayer Brushless DC Motor for Heavy Lift Drones," *Energies,* vol. 14, 2021.

[3] R. L. Valle, P. M. De Almeida, G. A. Fogli, A. A. Ferreira and P. G. Barbosa, "Simple and Effective Digital Control of a Variable-Speed Low Inductance BLDC Motor Drive," *IEEE Access,* vol. 8, p. 13240–13250, 2020.

[4] F. Kurtulus and E. Akboy, "A comparasion of the effects of different commutation techniques on acoustic noise in AFPM UAV motors," *Electrical Engineering,* April 2024.

[5] F. Marcolini, G. De Donato, F. Giulii Capponi, M. Incurvati and F. Caricchi, "Design of a Multiphase Coreless Axial Flux Permanent Magnet Machine for Unmanned Aerial Vehicle Propulsion," in *2020 IEEE Energy Conversion Congress and Exposition (ECCE)*, 2020.

[6] A. J. Kanapara and K. P. Badgujar, "Performance Improvement of Permanent Magnet Brushless DC Motor through Cogging Torque Reduction Techniques," in *2020 21st National Power Systems Conference (NPSC)*, 2020.

[7] D. Gerada, A. Mebarki, N. L. Brown, C. Gerada, A. Cavagnino and A. Boglietti, "High-Speed Electrical Machines: Technologies, Trends, and Developments," *IEEE Transactions on Industrial Electronics,* vol. 61, p. 2946–2959, June 2014.

[8] N. S., S. P. Nikam, S. Pal, A. K. Wankhede and B. G. Fernandes, "Performance Comparison Between PCB-Stator and Laminated-Core-Stator-Based Designs of Axial Flux Permanent Magnet Motors for High-Speed Low-Power Applications," *IEEE Transactions on Industrial Electronics,* vol. 67, p. 5269–5277, July 2020.

[9] J. Fang, X. Zhou and G. Liu, "Instantaneous Torque Control of Small Inductance Brushless DC Motor," *IEEE Transactions on Power Electronics,* vol. 27, p. 4952–4964, December 2012.

[10] A. Jaya, E. Purwanto, M. B. Fauziah, F. D. Murdianto, G. Prabowo and M. R. Rusli, "Design of PID-fuzzy for speed control of brushless DC motor in dynamic electric vehicle to improve steady-state performance," in *2017 International Electronics Symposium on Engineering Technology and Applications (IES-ETA)*, 2017.

[11] N. Moehle and S. Boyd, "Optimal current waveforms for brushless permanent magnet motors," *International Journal of Control,* vol. 88, p. 1389–1399, April 2015.

[12] S. Lee, T. Lemley and G. Keohane, "A comparison study of the commutation methods for the three-phase permanent magnet brushless DC motor," in *Electrical Manufacturing Technical Conference 2009*, 2009.

[13] STMicroelectronics, "Discovery kit with STM32G431CB MCU," [Online]. Available: https://www.st.com/en/evaluation-tools/b-g431b-esc1.html. [Accessed 10 12 2024].

[14] Diodes Incorporated, "AN1164: Introduction to Brushless DC Motors," 05 2021. [Online]. Available: https://www.diodes.com/assets/Uploads/AN1164-BLDC-Motors.pdf. [Accessed 23 09 2024].

[15] Lin Engineering Inc., "What is a Slotless Motor?," [Online]. Available: https://www.linengineering.com/what-is-a-slotless-motor. [Accessed 27 10 2024].

[16] B. A. Nasir, "An Accurate Iron Core Loss Model in Equivalent Circuit of Induction Machines," *Journal of Energy,* vol. 2020, p. 1–10, February 2020.

[17] Microchip Technology Inc, "Sensorless Field Oriented Control (FOC) of a Permanent Magnet Synchronous Motor (PMSM)," 2010. [Online]. Available: https://ww1.microchip.com/downloads/en/appnotes/01078b.pdf. [Accessed 23 09 2024].

[18] STMicroelectronics, "Sensorless six-step BLDC commutation - AN4220," 2013. [Online]. Available: https://www.st.com/resource/en/application_note/an4220-sensorless-sixstep-bldc-commutation-stmicroelectronics.pdf. [Accessed 24 09 2024].

[19] STMicroelectronics, "Current sensing in BLDC motor application - Application note," 2020. [Online]. Available: https://www.st.com/resource/en/application_note/an5423-current-sensing-in-bldc-motor-application-stmicroelectronics.pdf. [Accessed 23 09 2024].

[20] STMicroelectronics, "Sensorless BLDC motor control and BEMF sampling methods with ST7MC - AN1946," 2007. [Online]. Available: https://www.st.com/resource/en/application_note/cd00020086-sensorless-bldc-motor-control-and-bemf-sampling-methods-with--st7mc-stmicroelectronics.pdf. [Accessed 24 09 2024].

[21] T. Kim, H.-W. Lee and M. Ehsani, "Position sensorless brushless DC motor/generator drives: review and future trends," *IET Electric Power Applications,* vol. 1, p. 557–564, July 2007.

[22] , Texas Instruments Incorporated, "Sine Wave Generation Using PWM With Hercules N2HET and HTU," 05 2015. [Online]. Available: https://www.ti.com/lit/an/spna217/spna217.pdf?ts=1727358953811. [Accessed 26 09 2024].

[23] Texas Instruments 2011, "Motor Control Compendium," 2010. [Online]. Available: https://www.ti.com/download/trng/docs/c2000/TI_MotorControlCompendium_2010.pdf. [Accessed 27 09 2024].

[24] Y. Solbakken, "Space Vector PWM Intro," 01 05 2017. [Online]. Available: https://www.switchcraft.org/learning/2017/3/15/space-vector-pwm-intro. [Accessed 27 09 2024].

[25] A. Skuric, H. S. Bank, R. Unger, O. Williams and D. González-Reyes, "SimpleFOC: A Field Oriented Control (FOC) Library for Controlling Brushless Direct Current (BLDC) and Stepper Motors," *Journal of Open Source Software,* vol. 7, p. 4232, June 2022.

[26] J. C. Gamazo-Real, E. Vázquez-Sánchez and J. Gómez-Gil, "Position and Speed Control of Brushless DC Motors Using Sensorless Techniques and Application Trends," *Sensors,* vol. 10, p. 6901–6947, July 2010.

[27] J. Holtz, "Sensorless control of induction motor drives," *Proceedings of the IEEE,* vol. 90, p. 1359–1394, August 2002.

[28] K. Kolano, "New Method of Vector Control in PMSM Motors," *IEEE Access,* vol. 11, p. 43882–43890, 2023.

[29] Texas Instruments Incorporated, "Sensorless-FOC With Flux-Weakening and MTPA Motor Drives," 04 2018. [Online]. Available: https://www.ti.com/lit/an/spracf3/spracf3.pdf?ts=1729171481269&ref_url=https%253A%252F%252Fwww.google.com%252F. [Accessed 17 10 2024].

[30] Texas Instruments Incorporated, "DRV8316 Three-Phase Integrated FET Motor Driver datasheet (Rev. B)," 04 2022. [Online]. Available: https://www.ti.com/lit/ds/symlink/drv8316.pdf. [Accessed 14 12 2024].

[31] Heatsink Calculator, "PCB Temperature Calculator," [Online]. Available: https://www.heatsinkcalculator.com/pcb-temperature-calculator.html. [Accessed 15 12 2024].

[32] Same Sky, "HSB02-101007 Datasheet," 12 09 2024. [Online]. Available: https://www.sameskydevices.com/product/resource/hsb02-101007.pdf. [Accessed 15 12 2024].

[33] D. Molony, "MESC_Firmware," [Online]. Available: https://github.com/davidmolony/MESC_Firmware/. [Accessed 15 12 2024].

[34] simplefoc, "Arduino-FOC-drivers," [Online]. Available: https://github.com/simplefoc/Arduino-FOC-drivers. [Accessed 15 12 2024].

[35] Adafruit, "Adafruit_NeoPixel," [Online]. Available: https://github.com/adafruit/Adafruit_NeoPixel. [Accessed 17 12 2024].

[36] APC Propellers, "APC Propeller Performance Data," [Online]. Available: https://www.apcprop.com/technical-information/performance-data/. [Accessed 13 12 2024].

APPENDICES

Appendix 1 ESC schematic

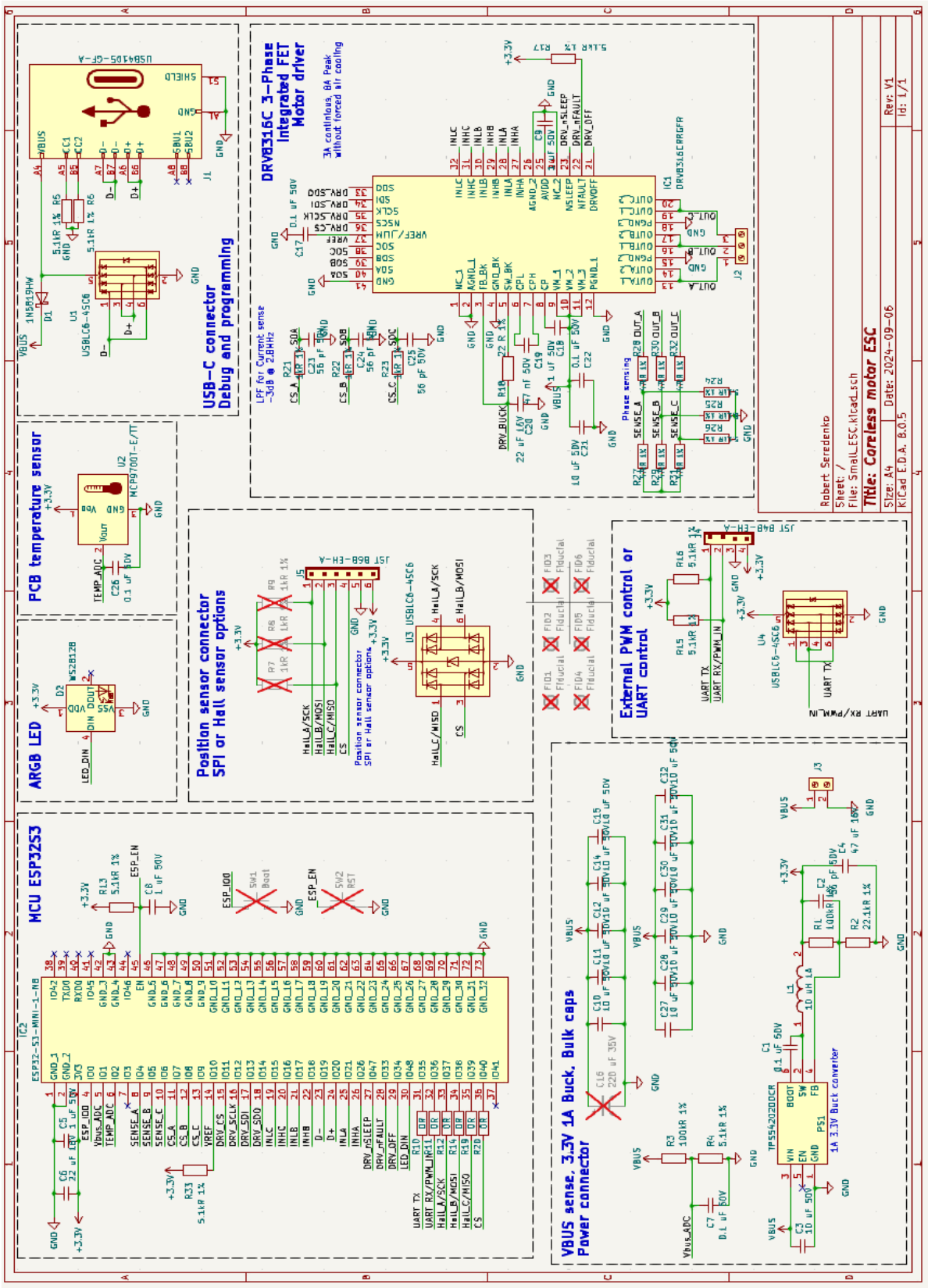

Appendix 2 MATLAB Simulink model of 6-step and FOC ESC

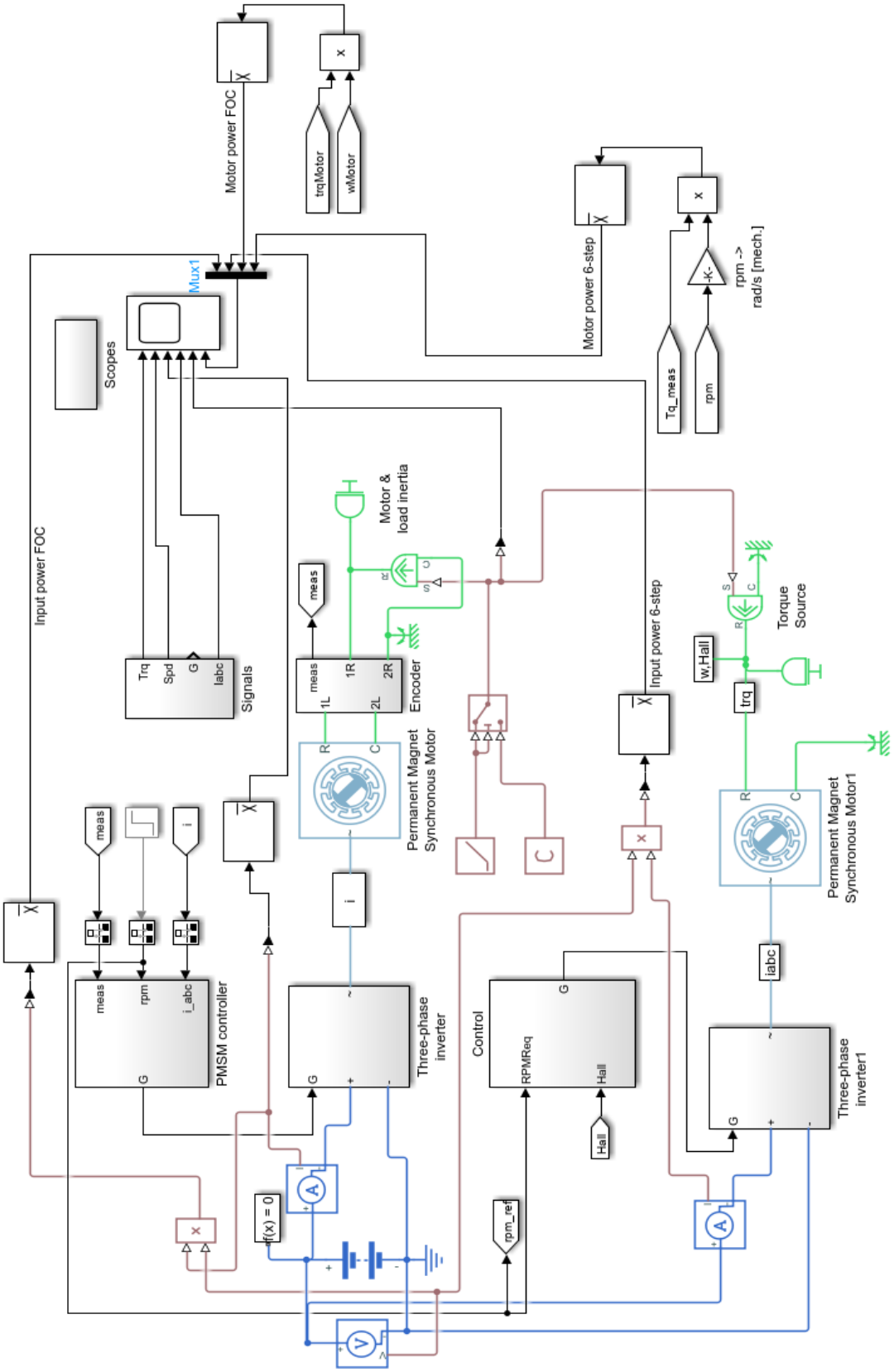

Appendix 3 GitHub repository for prototype FOC ESC

Hardware design files and all firmware files are available from the QR-code below or from the GitHub link:
https://github.com/Sp1kys/Sensorless_Coreless_motor_ESC_SimpleFOC